

THE INFLUENCE OF A CENTRAL GROOVE ON STATIC AND
DYNAMIC CHARACTERISTICS OF AN ANNULAR LIQUID SEAL
WITH LAMINAR FLOW

A Thesis

by

MATTHEW SHERIDAN GRAVISS

Submitted to the Office of Graduate Studies of
Texas A&M University
in partial fulfillment of the requirements for the degree of

MASTER OF SCIENCE

May 2005

Major Subject: Mechanical Engineering

THE INFLUENCE OF A CENTRAL GROOVE ON STATIC AND
DYNAMIC CHARACTERISTICS OF AN ANNULAR LIQUID SEAL
WITH LAMINAR FLOW

A Thesis

by

MATTHEW SHERIDAN GRAVISS

Submitted to Texas A&M University
in partial fulfillment of the requirements
for the degree of

MASTER OF SCIENCE

Approved as to style and content by:

Dara W. Childs
(Chair of Committee)

Luis A. San Andrés
(Member)

Charles E. Harris
(Member)

Dennis L. O'Neal
(Head of Department)

May 2005

Major Subject: Mechanical Engineering

ABSTRACT

The Influence of a Central Groove on Static and Dynamic Characteristics of an Annular
Liquid Seal with Laminar Flow. (May 2005)

Matthew Sheridan Graviss, B.M.E., Auburn University

Chair of Advisory Committee: Dr. Dara W. Childs

This thesis provides experimental static and dynamic results for four pairs of seals, including a pair of smooth seals and three pairs of centrally grooved seals. The grooved seals have groove depth to clearance ratios (D_g/C) of 5, 10, and 15. The radial clearance of each test seal is 0.0891 mm. Test conditions include three shaft rotational speeds from 4000 to 10000 rpm, three inlet oil pressures from 24 to 70 bars, and seal dimensionless eccentricities from 0 (centered) to 0.7. For each pair of test seals, dynamic results include stiffness and damping coefficients; static results include stator position, attitude angles, and seal leakage. Stiffness, damping, and leakage are compared among the seal pairs with various groove depths. Results show that all rotordynamic coefficients consistently decrease with increasing seal groove depths, and seal leakage remains constant through varying groove depths. Additionally, a comparison is made between experimental results of all test seals and XLLubeGT. XLLubeGT is a computer model developed at Texas A&M University, which uses a Reynolds equation + energy equation model to predict dynamic performance of a grooved seal. It operates on the assumption that the groove is large enough to create separate lands within the seal, creating a zero or negligible pressure perturbation across the seal. A comparison with XLLubeGT shows that even the seal with the largest groove depth tested is not deep enough to agree with XLLubeGT predictions.

TABLE OF CONTENTS

	Page
ABSTRACT	iii
TABLE OF CONTENTS	iv
LIST OF FIGURES	v
LIST OF TABLES	vii
NOMENCLATURE	viii
INTRODUCTION	1
LITERATURE REVIEW	4
TEST RIG DESCRIPTION	8
Main Components	8
Loading Configuration	9
Instrumentation	11
Seal Geometry	12
EXPERIMENTAL PROCEDURE AND PARAMETER IDENTIFICATION	14
Parameter Identification	15
Uncertainty Analysis and Curve Fitting Procedure	17
STATIC PERFORMANCE	20
DYNAMIC PERFORMANCE CHARACTERISTICS	24
Measurement of Baseline	24
Seal Dynamic Stiffness	25
EXPERIMENTAL RESULTS AND PREDICTIONS	28
Influence of Groove Depth	28
XLTRC ² – XLLubeGT	38
Seal Leakage	44
Whirl Frequency Ratio (WFR)	46
Impact of Clearance on XLLubeGT Predictions	48
CONCLUSIONS	52
REFERENCES	55
APPENDIX	58
VITA	61

LIST OF FIGURES

	Page
Figure 1. Typical assembly of a multi-ring seal	1
Figure 2. General test seal design.....	2
Figure 3. Geometric detail of a circumferentially grooved seal.....	2
Figure 4. Bearing test rig main test section.....	8
Figure 5. Shaker configuration.....	10
Figure 6. Static loader assembly	11
Figure 7. Sensor locations in the stator section.....	12
Figure 8. Seal geometry (all dimensions in millimeters)	13
Figure 9. Groove detailed dimensions for seals to be tested (all dimensions in millimeters)	13
Figure 10. Coordinate reference frame	15
Figure 11. Seal centerline loci plots for three inlet pressures (LP, MP, HP) at an operating speed of 7000 rpm for a $D_g/C = 10$	21
Figure 12. Attitude angle versus unit load for three inlet pressures (LP, MP, HP) at an operating speed of 7000 rpm for a $D_g/C = 10$	22
Figure 13. Attitude angle versus Sommerfeld number for three inlet pressures (LP, MP, HP) at an operating speed of 7000 rpm for a $D_g/C = 10$	23
Figure 14. Seal leakage versus eccentricity ratio for (a) 7000 rpm and varying pressures (LP, MP, HP) and (b) 45 bars and varying speeds (4000, 7000, 10000 rpm)	23
Figure 15. Baseline dynamic stiffness.....	24
Figure 16. Real direct and cross-coupled dynamic stiffness at 10000 rpm, 70 bars, and ϵ of 0.5	25
Figure 17. Imaginary direct dynamic stiffness at 10000 rpm, 70 bars, and ϵ of 0.5	26
Figure 18. Cross-coupled stiffness (K_{xy}) versus eccentricity for all test seals and three inlet oil pressures.....	29
Figure 19. Direct stiffness in the x-direction versus eccentricity for each rotor speed....	30
Figure 20. Direct stiffness in the y-direction versus eccentricity for each rotor speed....	30
Figure 21. Cross-coupled stiffness (K_{xy} and K_{yx}) versus eccentricity for each rotor speed.....	31

	Page
Figure 22. Direct damping in the y-direction vs. eccentricity at 7000 rpm for oil inlet pressures of (a) 24 bars (b) 45 bars (c) 70 bars	32
Figure 23. Direct damping in the x-direction versus eccentricity for each rotor speed ...	33
Figure 24. Direct damping in the y-direction versus eccentricity for each rotor speed ...	33
Figure 25. Cross-coupled damping (C_{xy} and C_{yx}) vs. eccentricity for each rotor speed ..	34
Figure 26. Direct added mass in the x-direction for all test rotor speeds and oil inlet pressures	36
Figure 27. Direct added mass in the y-direction for all test rotor speeds and oil inlet pressures	37
Figure 28. Coordinate frame for (a) experiments and (b) XLLubeGT	40
Figure 29. Stiffness and damping coefficients versus oil inlet pressure at $\varepsilon = 0.3$: experimental ($D_g/C = 15$) vs. theory	42
Figure 30. Direct and cross-coupled stiffness coefficients (a) K_{xx} (b) K_{yy} (c) K_{xy} (d) K_{yx} versus eccentricity (0, 0.3, 0.5, 0.7)	43
Figure 31. Direct and cross-coupled damping coefficients (a) C_{xx} (b) C_{yy} (c) C_{xy} (d) C_{yx} versus eccentricity (0, 0.3, 0.5, 0.7)	44
Figure 32. Leakage versus eccentricity for all test speeds and oil inlet pressures	45
Figure 33. WFR vs. eccentricity for all test conditions of speed, oil inlet pressure, and groove depth	47
Figure 34. Comparison of direct and cross-coupled stiffness coefficients between XLLubeGT predictions with and without growth analyses	49
Figure 35. Comparison of direct and cross-coupled damping coefficients between XLLubeGT predictions with and without growth analyses	50
Figure 36. Comparison of seal leakage rates among XLLubeGT predictions with and without growth analyses, and experimental data from $D_g/C=15$	51
Figure 37. Direct and cross-coupled stiffness coefficients (a) K_{xx} (b) K_{yy} (c) K_{xy} (d) K_{yx} versus eccentricity (0, 0.3, 0.5)	59
Figure 38. Direct and cross-coupled damping coefficients (a) C_{xx} (b) C_{yy} (c) C_{xy} (d) C_{yx} versus eccentricity (0, 0.3, 0.5)	60

LIST OF TABLES

	Page
Table 1. Measured radial seal clearances	12
Table 2. Nominal test matrix for static and dynamic tests	14
Table 3. Maximum Reynolds numbers for different rotor speeds	39

NOMENCLATURE

A_{ij}	Fourier transforms for the measured stator acceleration. (e.g. A_{ij} is the acceleration in “j” direction, due to an excitation force in the “i” direction) [m/s^2]
C_{ij}	Direct and cross-coupled damping coefficients [N.s/m]
ΔC_{ij}	Uncertainty of direct and cross-coupled damping coefficients [N.s/m]
C	Radial seal clearance [m]
c_p	Lubricant specific heat [$\text{J}/(\text{kg.K}^0)$]
D	Seal diameter [m]
D_g	Seal groove depth [m]
D_{ij}	Fourier transforms for the measured stator relative motion [m]
E	Modulus of elasticity [N/m^2]
F_{ij}	Fourier transforms for the measured stator force [N]
F_s	Applied static load in the positive y-direction [N]
$f_{sx} f_{sy}$	Seal reaction force component in the x,y direction respectively [N]
$f_x f_y$	Measured excitation force component in the x,y direction [N]
\mathbf{H}_{ij}	Direct and cross-coupled dynamic stiffness [N/m]
\mathbf{j}	Imaginary unit, $\sqrt{-1}$ [-]
\mathbf{K}_{ij}	Direct and cross-coupled stiffness coefficients [N/m]
$\Delta \mathbf{K}_{ij}$	Uncertainty of direct and cross-coupled stiffness coefficients [N/m]
L	Seal length [m]
M_s	Mass of the stator [kg]
M_{ij}	Direct and cross-coupled added-mass coefficients [kg]
ΔM_{ij}	Uncertainty of added-mass coefficients [kg]
N	Rotor speed [Hz]
R	Seal radius [m]
Re	Reynolds number [-]

R_g	Seal groove radius [m]
R_r	Rotor radius [m]
T_{avg}	Average of T_{in} and T_{out} [$^{\circ}K$]
T_{in}	Oil inlet temperature [$^{\circ}K$]
T_{out}	Oil outlet temperature (average of the NDE and DE temperatures) [$^{\circ}K$]
W_g	Seal groove width [m]
$\ddot{x}_s \ddot{y}_s$	Absolute acceleration of the stator in the x,y direction [m/s^2]
$\Delta x \Delta y$	Relative motion between the rotor and the stator in the x,y directions [m]

Greek Symbols

α	Thermal expansion coefficient [in/in $^{\circ}C$]
Λ	The square of the excitation frequency, $\Omega^2 [(1/s)^2]$
ε_o	Eccentricity ratio [-]
μ_{Tave}	Viscosity at the average temperature [$N.s/m^2$]
ν	Poisson's ratio [-]
ϕ	Attitude angle [degree]
ρ	Lubricant density [kg/m^3]
ρ_r	Rotor density [kg/m^3]
ω	Running speed of rotor [rpm]
Ω	Excitation frequency of stator [Hz]
ω_s	Onset speed of instability [rpm]

Subscripts

x,y	x and y direction (defined in Figure 10)
i,j	x,y

Abbreviations

rpm	Revolutions per minute
-----	------------------------

DE, NDE Drive end, non-drive end
ID, OD Seal inner and outer diameter
LP, MP, HP Low, medium, and high oil inlet pressures for figure notation

INTRODUCTION

Oil bushing seals are generally used to reduce the flow of lubrication fluids in compressors and keep the gas in the compressor [1]. Current developments in turbomachinery include the following factors: increased speeds, efficiency, pressure, and additional stages. Oil seals have a significant impact on the rotordynamic stability of a compressor. Additionally, accurate modeling of oil seals has proven to be important in examining their effect on system dynamic stability and rotor response [1].

Figure 1 represents a cross-sectional view of a typical multi-ring oil seal cartridge assembly. The inner and outer seals are preloaded by a spring to maintain a proper seal position. As oil enters the system, it moves from a high pressure region to a low pressure region in both the inner and outer seals, creating the sealant effect [2].

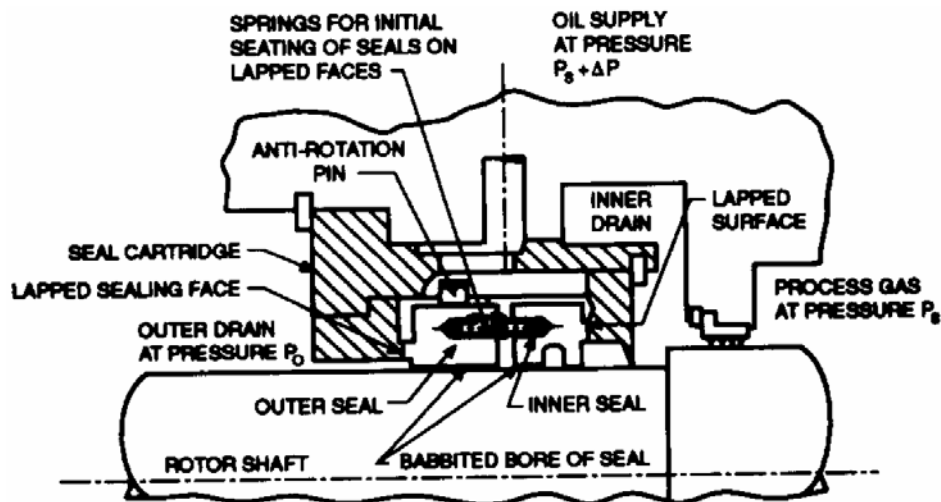


Figure 1. Typical assembly of a multi-ring seal [1]

The geometry of a seal is very straightforward. Although groove geometry may change with each test seal, the main geometry remains the same. Figure 2 shows the

basic geometry for a laminar flow, circumferentially grooved oil seal. The test seals used here are manufactured from 660 bearing bronze.

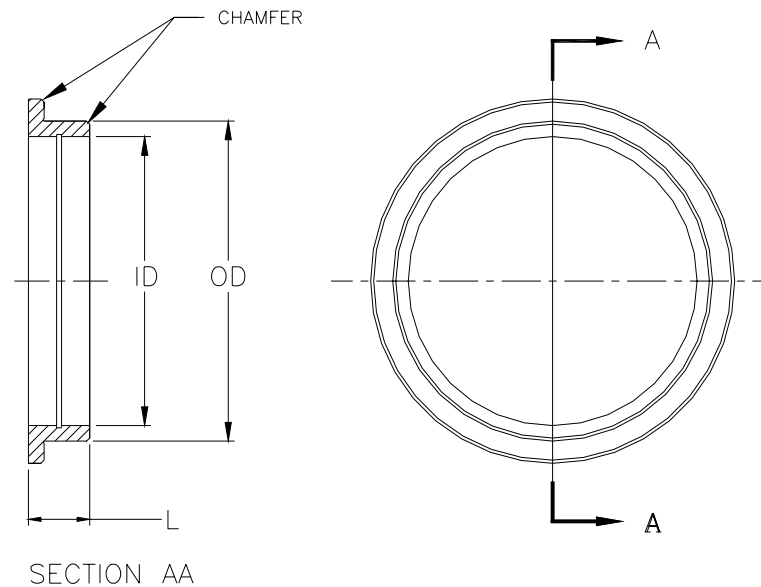


Figure 2. General test seal design

Figure 3 depicts the detailed geometry of a square groove and a semicircular groove, the two most common groove shapes. Both are representative of industrial practice.

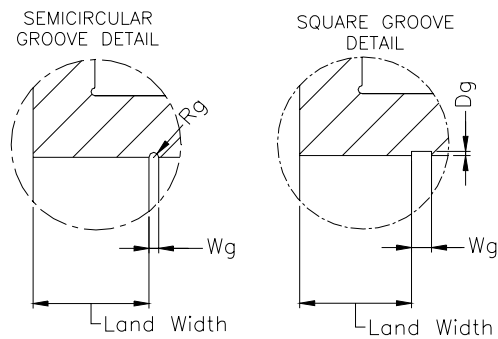


Figure 3. Geometric detail of a circumferentially grooved seal

Oil bushing seals are generally located near tilting-pad bearings. The oil bushing seals have significant cross-coupled stiffness coefficients. Tilting-pad bearings have no cross-coupled stiffness and considerably more damping than the oil seals. Grooving the oil seals reduces the combined cross-coupled stiffness considerably, but only reduces the combined direct damping a little. This can be represented by the combined whirl frequency ratio (*WFR*) of the bearings and seals:

$$WFR(Combined) = \frac{k(combined)}{C(combined) \times \omega} \quad (1)$$

WFR is a commonly used parameter for evaluating the stability characteristics of a bearing. It is defined as the ratio between the rotor whirl frequency and the shaft speed at which the system becomes unstable.

Childs et al. [3] show that the circumferential groove geometry used for their investigation, a circular cross section with radius 0.508 mm (0.02 in), does not provide any significant difference in stiffness and damping between the 1-groove, 3-groove, and plain annular seal. This led to the conclusion that the groove geometry used was not effective in creating separate lands within the seal. This finding contradicts grooved-seal code predictions.

The primary goal of this research project is to determine how large and deep a groove should be to become effective and produce zero or negligible pressure perturbations due to rotor motion. To answer this question, a one-groove seal is tested using a groove width of 2.032 mm (0.080 in), with varying groove depths of 0.4216 mm (0.0166 in), 0.8407 mm (0.0331 in), and 1.26238 mm (0.0497 in). The diametral clearance of the seal with respect to the rotor is 0.1782 mm (0.0067 in). This proposed research determines rotordynamic coefficients at three speeds, four eccentricities, and three flow pressures.

LITERATURE REVIEW

Literature pertinent to the proposed research can be divided into two primary categories: turbulent-flow oil seals and laminar-flow oil seals. Turbulent-flow annular seals have a low viscosity, a high pressure differential, and a large clearance-to-radius ratio [4]. Laminar-flow oil seals generally have smaller clearances and higher lubricant viscosities. Because of these differences, the following two methods are used for the prediction of seal behavior: (i) the bulk-flow Navier –Stokes model, and (ii) the Reynolds equation model. The attributes of a turbulent-flow oil seal create a high Reynolds number ($Re > 2000$), and therefore, the bulk-flow Navier –Stokes model is appropriate. Conversely, the attributes of a laminar-flow oil seal produce a low Reynolds number, and the basic Reynolds equation model is more applicable.

Lomakin [5] was the first to analyze the effect a turbulent-flow seal has on system stability in a pump. The model used for this analysis neglected shaft rotation and lateral velocity. Lomakin developed “an analytical solution for direct stiffness based on changes in the dynamic pressure distribution caused by a small rotor displacement from a centered position.”

A bulk-flow model was used by Black [6] to analyze the effect of hydraulic forces in turbulent annular seals. Black first develops equations for the direct rotordynamic coefficients (stiffness, damping, and inertia). Black then determines the seal’s force on the shaft by integrating the pressure distribution over the surface of the shaft. Black and Jenssen [7] added to Black’s previous analysis by providing the additional prediction of cross-coupled rotordynamic coefficients. Black and Cochrane [8] then developed a model for circumferentially-grooved seals that developed predictions of dynamic coefficients. Each of Black’s analyses used turbulent-flow models. As previously stated, Black uses a bulk-flow model, which is suitable for turbulent flow seals.

In 1992, Wilkes, Kirk, and Elrod [9] provide an analysis of rotordynamic forces developed in circumferentially grooved annular seals. They compared theoretical

predictions with experimental results. Predictions were based on Hirs' theory for turbulent lubrication films using a bulk-flow model [10]. Experimental results used for this analysis were taken from Childs [11]. Both experimental and predicted results show that adding circumferential grooves to a seal decreases leakage and enhances stability.

In a paper analyzing multi-land high-pressure oil seals, Semanate and San Andrés [2] develop a model that predicts static and dynamic force coefficients. The analysis is based on a fully developed bulk-flow model for low axial Reynolds numbers. One, two, and three-grooved seals are examined for rotordynamic coefficients and load capacity. They determined that the smooth seal has a greater load capacity than the grooved seals. Semanate and San Andrés show that the smooth seals provide a lower leakage than the multi-land seals. This is due to the fact that “the presence of grooves inhibits the advancement of the hydrodynamic effect and reduces the overall fluid flow resistance.”

Semanate and San Andrés note that, as the journal eccentricity increases, this difference between the smooth and grooved seals increases. Also, the rotordynamic coefficients of the smooth seal are larger than those of the grooved seals. This difference widens as the eccentricity increases. As far as stability analysis, the authors showed that there is not improved stability with the addition of grooves. This result was based on the finding that the reduction of both the direct damping and the cross-coupled stiffness is proportional. Another primary conclusion from their research is that for laminar oil seals, “the entrance loss viscous effect can substantially increase the direct stiffness.”

Iwatsubo and Yang [12] analyze the effect of elastic deformation, due to high pressure, on the static and dynamic characteristics of turbulent-flow plain annular seals. Results showed that the direct stiffness in the x-direction is considerably influenced by elastic deformation. Also, the damped critical speeds of the first and second modes increase due to the elastic deformation. Results also showed little change in the other rotordynamic coefficients.

In 1996, Venkataraman and Palazzolo [13] developed a theory for analyzing the effect of wall flexibility on the rotordynamic coefficients of turbulent annular seals. They used an axi-symmetric, iso-parametric finite element formulation of the seal wall to determine wall deformation. A bulk-flow, turbulent, variable properties model was used to develop the flow field. The thermo-elasto-hydrodynamic model developed shows that the effect of wall flexibility may be significant for seals with large pressure drops, but negligible for those seals under only low pressure. Venkataraman and Palazzolo also show that wall flexibility also causes rotordynamic coefficients to be frequency dependent.

Recent papers preceding the proposed research are by Childs et al. [3]. In 2003, a series of seals was tested using the same test rig that will be used for this research. Three seals were tested: smooth, one-groove, and three-groove. The one-groove and the three-groove seals had the same groove geometry. A semicircular groove geometry was used for the one and three-grooved seals. Test conditions included three speeds, four eccentricities, and three oil supply pressures. Rotordynamic coefficients and static characteristics were determined.

XLLubeGT, a computer code developed by Dr. San Andrés of Texas A&M University, was created to analyze the rotordynamic coefficients of laminar oil bushing seals with smooth and circumferentially grooved geometries. XLLubeGT is based on a Reynold's equation model plus the energy equation for temperature predictions. The model was developed assuming that the grooves in the seals are large enough to create separate lands within the seals, yielding zero groove pressure perturbations. Based on this assumption, seals with grooves are predicted to have considerably lower stiffness and damping coefficients and load capacity in comparison to a smooth seal.

Test results of Childs et al. [3] show that the dynamic coefficients and load capacity vary only slightly between the smooth, one-groove, and three-groove seals. These results suggest that the groove geometries provided were ineffective in creating zero pressure perturbation within the groove. These findings contradict the code results, which show a significant effect of the grooves on stiffness and damping. The results of

this testing produced the question: How does the geometry of the groove affect the rotordynamic coefficients and load capacity?

TEST RIG DESCRIPTION

Main Components

The test rig used to measure static and dynamic performance of oil seals is located at the Texas A&M Turbomachinery Laboratory. Figure 4 shows a sectional view of the test rig described by Kaul [14].

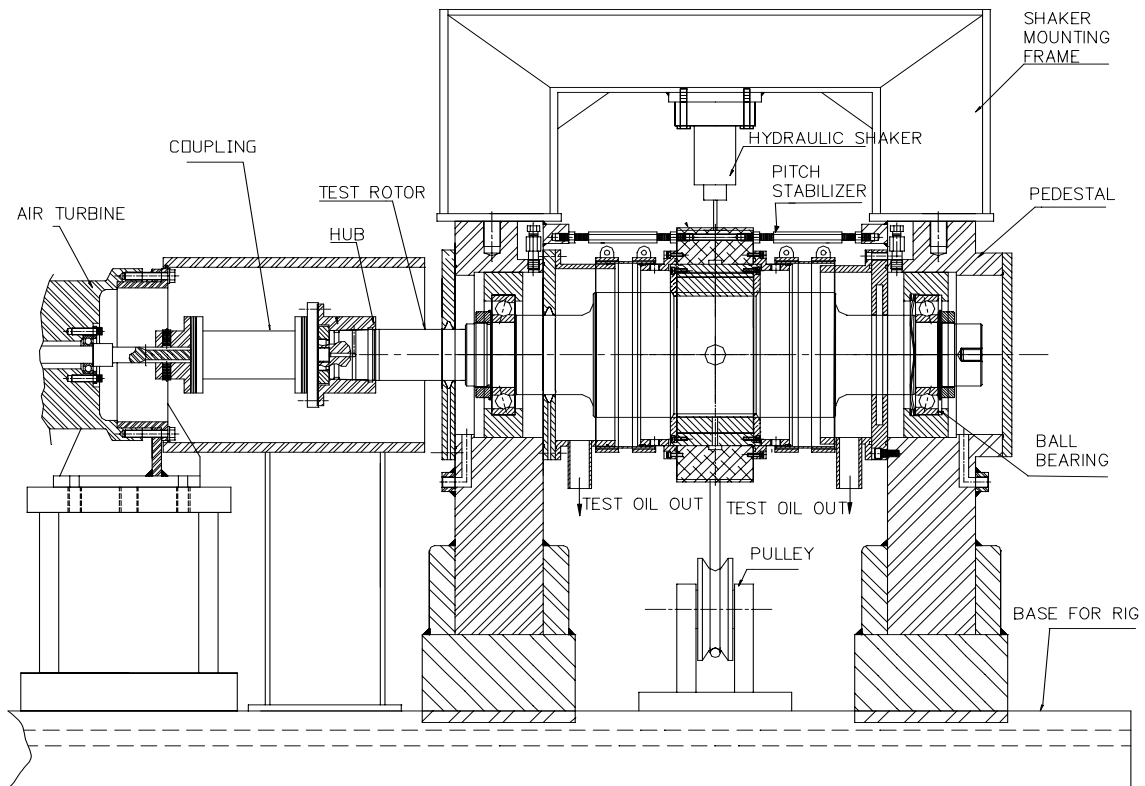


Figure 4. Bearing test rig main test section

The test apparatus is mounted on a steel base to ensure a level-operating surface and uses two pedestals, 381 mm (15 in) apart, which house the ball bearings that support the test rotor. An oil-mist system lubricates the ball bearings. The test rotor has an operating speed capability of 17,000 rpm, which is provided by a 65 kW-power air

turbine. The shaft is attached to the air turbine by a high-speed flexible disc coupling. The stainless steel shaft is machined to 116.8 mm (4.5988 in) diameter at the seal locations.

A pair of seals is housed in a stator, which also holds all temperature, pressure, acceleration, and motion instrumentation. Six pitch stabilizers ensure angular alignment between the stator and rotor. Static loads are applied to the stator by a pneumatic piston through a spring and pulley system. Using two hydraulic shakers positioned orthogonally from one another, dynamic loads are applied to the stator.

The oil supply system delivers ISO VG32 turbine oil to the test section. The lubricant has a viscosity of 0.02 Pa-s, and a density of 850 kg/m³ (note that the viscosity is temperature dependent). The maximum pressure and volumetric flow rate capacity of the system are 82.7 bars and 75 liters per minute, respectively.

Loading Configuration

Each hydraulic shaker is mounted to the stator middle section through a stinger, which isolates the test structure from the dynamics of the shakers structure. The locations of the shakers are depicted, from the non-drive end, in Figure 5. The shaker in the x-direction can excite the stator with dynamic loads up to 4450 N (1000 lbf) in tension and compression, and the shaker in the y-direction can excite the stator with dynamic loads up to 4450 N (1000 lbf) in tension and 11125 N (2500 lbf) in compression. Both shakers can excite the stator at frequencies up to 1000 Hz. The dynamic load is measured by load cells, which are located between the shaker heads and the stingers. The shakers, though capable of applying static loads, are exclusively used to provide dynamic loads.

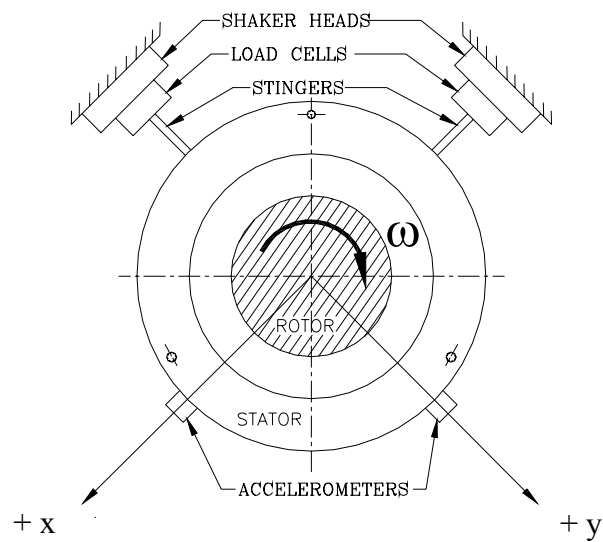


Figure 5. Shaker configuration

Figure 6 shows the static loader assembly. The static load is applied in the positive y-direction. A cable is connected to the stator assembly through a pulley and a yoke. A spring system connects the cable and the pneumatic cylinder. This system assures that the static load is applied exclusively in the y-direction. A load cell, attached to the cable, measures the static load. The rated maximum available load is 22000 N (5000 lbf).

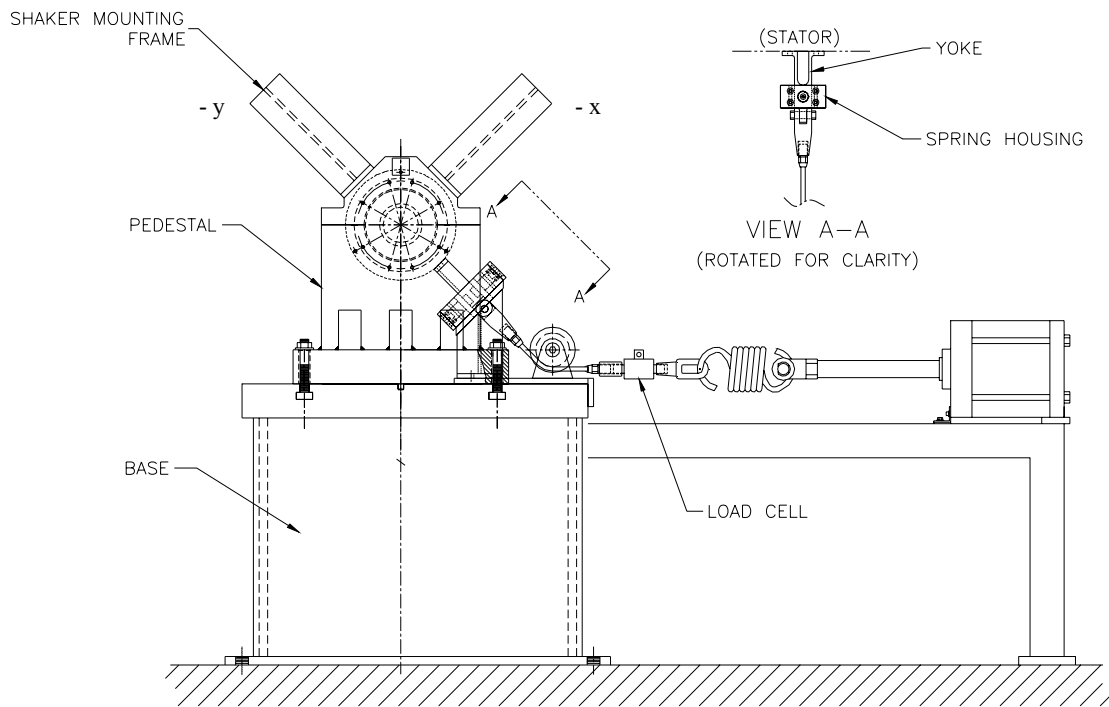


Figure 6. Static loader assembly

Instrumentation

Six eddy-current displacement sensors, located in the stator end caps, record the relative motion of the stator with respect to the rotor for each direction of excitation. Two proximity probes are provided in a plane (one per x and y directions) at the non-drive end (NDE). Four probes are located at a parallel plane (two per x and y directions), at the drive end (DE): two of the probes are used in conjunction with the two probes from the NDE to measure the pitch and yaw of the stator, while the remaining two proximity probes provide feedback to the shakers' control system.

Piezoelectric accelerometers measure the stator absolute acceleration in the x and y directions. Pressure and temperature probes are located in the oil-inlet chamber as well as at both end caps. Figure 7 shows the location of all measurement probes. Oil is

supplied at the stator mid-plane and exits between the seals and the rotor to oil discharge chambers located on both the DE and NDE sides of the stator.

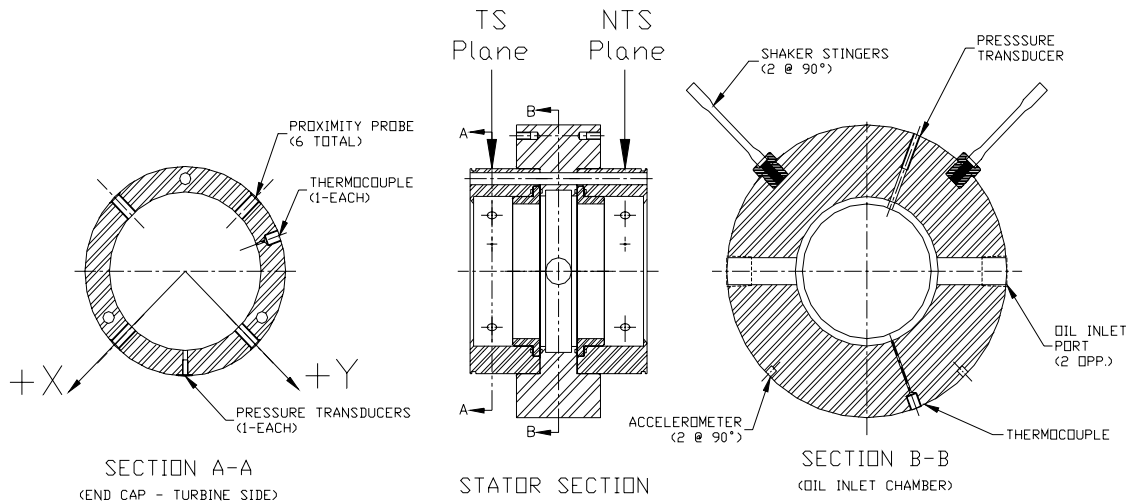


Figure 7. Sensor locations in the stator section

Seal Geometry

The seal geometry is shown in Figure 8. One pair of seals tested is smooth, while the other three pairs have a circumferential groove. The groove depths to clearance ratios, D_g/C , to be tested are 0, 5, 10, and 15. The groove detail dimensions are given in Figure 9. Also,

Table 1 details the measured radial clearance for each set of seals.

Table 1. Measured radial seal clearances

Seal	C*
$D_g/C = 0$	0.0851 mm (3.36 in $\times 10^{-3}$)
$D_g/C = 5$	0.0856 mm (3.37 in $\times 10^{-3}$)
$D_g/C = 10$	0.0851 mm (3.35 in $\times 10^{-3}$)
$D_g/C = 15$	0.0859 mm (3.38 in $\times 10^{-3}$)

* Measurements made at 25 °C (77°F)

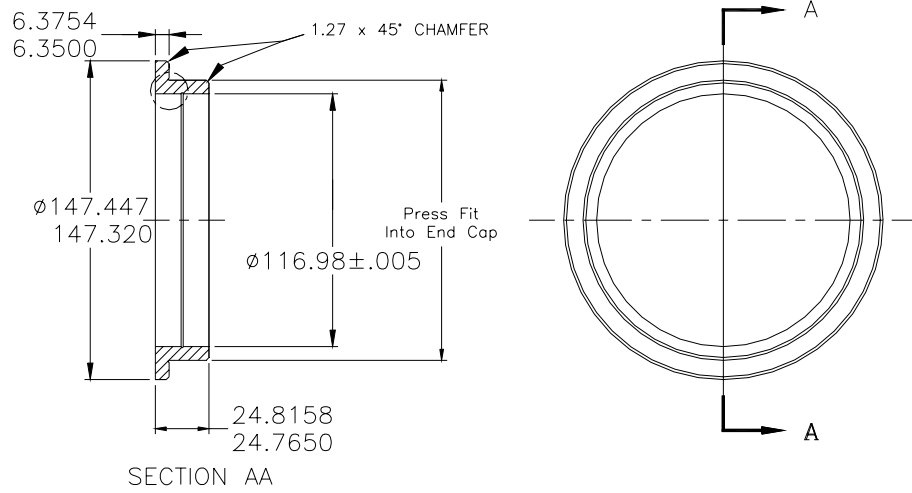


Figure 8. Seal geometry (all dimensions in millimeters)

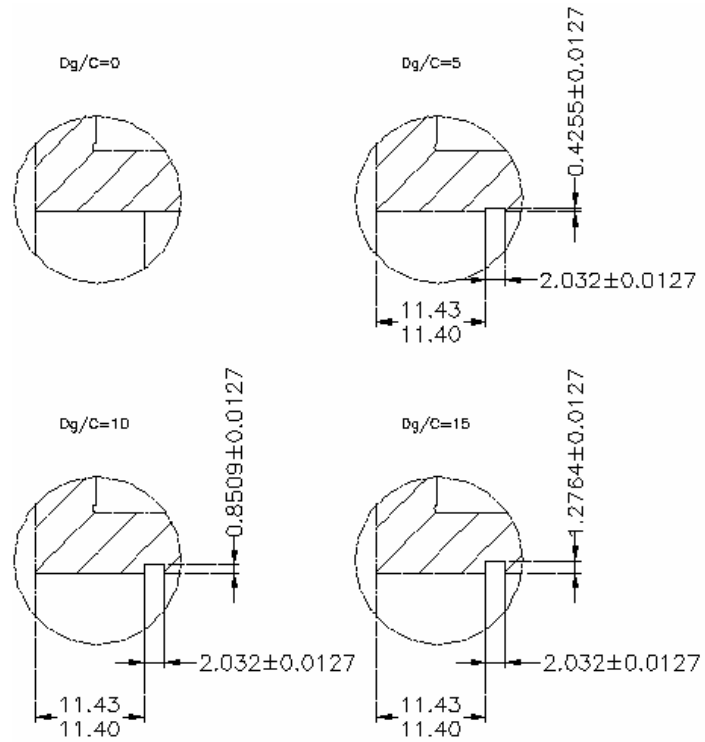


Figure 9. Groove detailed dimensions for seals to be tested (all dimensions in millimeters)

EXPERIMENTAL PROCEDURE AND PARAMETER IDENTIFICATION

Table 2 shows the test conditions at which static and dynamic data are taken. Upon reaching steady state conditions of shaft speed and static load, testing begins. A test is performed by shaking the stator in the x direction, and then in the y direction. The shakers excite the system using a pseudo-random dynamic excitation with frequencies from 20 to 220 Hz in 10 Hz increments.

Table 2. Nominal test matrix for static and dynamic tests

Rotor Speed rpm	Oil Inlet Pressure Bars (Psi)	Eccentricity			
		0	0.3	0.5	0.7
4000	24 (350)	X	X	X	X
	45 (650)	X	X	X	X
	70 (1000)	X	X	X	X
7000	24 (350)	X	X	X	X
	45 (650)	X	X	X	X
	70 (1000)	X	X	X	X
10000	24 (350)	X	X	X	X
	45 (650)	X	X	X	X
	70 (1000)	X	X	X	X

Static data obtained for each test include seal position with respect to the shaft, oil inlet and outlet temperatures, static loads and oil flow-rate data. Dynamic data include load applied by the shakers and absolute acceleration of the seal stator.

Parameter Identification

This section details the rotordynamic parameter identification procedure and has been adapted from Childs and Hale [15]. Though the parameter identification procedure used by Childs and Hale is for bearings, the method for calculating the rotordynamic coefficients of a pair of seals remains the same. The only difference for the seal test rig is that the resulting rotordynamic coefficients calculated will represent values for two seals combined. Therefore, the results will be divided by two in order to represent the rotordynamic coefficients of one seal. The equations of motion for the seal stator mass M_s can be written as:

$$M_s \begin{bmatrix} a_x \\ a_y \end{bmatrix} = \begin{bmatrix} f_x \\ f_y \end{bmatrix} + \begin{bmatrix} f_{sx} \\ f_{sy} \end{bmatrix}, \quad (2)$$

where a_x and a_y are the measured components of the stator's acceleration, f_x and f_y are the measured excitation forces, and f_{sx} and f_{sy} are the seal reaction force components. The x and y subscripts in these equations identify the x and y direction, as depicted in Figure 10.

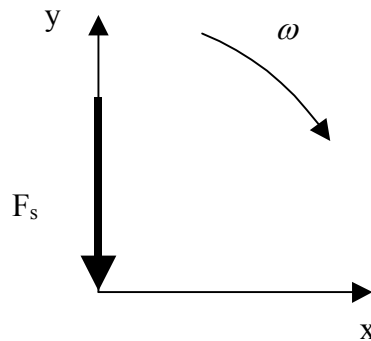


Figure 10. Coordinate reference frame

The seal reaction force is correlated to the rotordynamic coefficients by:

$$-\begin{bmatrix} f_{sx} \\ f_{sy} \end{bmatrix} = \begin{bmatrix} K_{xx} & K_{xy} \\ K_{yx} & K_{yy} \end{bmatrix} \begin{bmatrix} \Delta x \\ \Delta y \end{bmatrix} + \begin{bmatrix} C_{xx} & C_{xy} \\ C_{yx} & C_{yy} \end{bmatrix} \begin{bmatrix} \Delta \dot{x} \\ \Delta \dot{y} \end{bmatrix} + \begin{bmatrix} M_{xx} & M_{xy} \\ M_{yx} & M_{yy} \end{bmatrix} \begin{bmatrix} \Delta \ddot{x} \\ \Delta \ddot{y} \end{bmatrix}, \quad (3)$$

where $\Delta x, \Delta y$ are defined as the relative motion between the rotor and the stator, and the subscripts (xx, yy) and (xy, yx) refer to the direct and cross-coupled terms, respectively. Substitution Eq. (2) into Eq. (3), it follows that

$$\begin{bmatrix} f_x - M_s \ddot{x}_s \\ f_y - M_s \ddot{y}_s \end{bmatrix} = \begin{bmatrix} K_{xx} & K_{xy} \\ K_{yx} & K_{yy} \end{bmatrix} \begin{bmatrix} \Delta x \\ \Delta y \end{bmatrix} + \begin{bmatrix} C_{xx} & C_{xy} \\ C_{yx} & C_{yy} \end{bmatrix} \begin{bmatrix} \Delta \dot{x} \\ \Delta \dot{y} \end{bmatrix} + \begin{bmatrix} M_{xx} & M_{xy} \\ M_{yx} & M_{yy} \end{bmatrix} \begin{bmatrix} \Delta \ddot{x} \\ \Delta \ddot{y} \end{bmatrix} \quad (4)$$

The left hand vector of Eq. (4) is a known function of time. On the right hand side, $\Delta x(t)$ and $\Delta y(t)$ are measured functions of time. The rotordynamic coefficients are determined in the frequency domain via the Fast Fourier Transform which gives

$$\begin{bmatrix} F_x - M_s A_x \\ F_y - M_s A_y \end{bmatrix} = \begin{bmatrix} \mathbf{H}_{xx} & \mathbf{H}_{xy} \\ \mathbf{H}_{yx} & \mathbf{H}_{yy} \end{bmatrix} \begin{bmatrix} D_x \\ D_y \end{bmatrix} \quad (5)$$

The elements of the seal frequency response function \mathbf{H}_{ij} in Eq. (5) are related to the coefficients defined in Eq. (4) by

$$\begin{aligned} \mathbf{H}_{ij} &= (K_{ij} - \Omega^2 M_{ij}) + j (\Omega C_{ij}), \\ \text{Re}(\mathbf{H}_{ij}) &= K_{ij} - \Omega^2 M_{ij}, \text{ and } \text{Im}(\mathbf{H}_{ij}) = \Omega C_{ij} \end{aligned} \quad (6)$$

Eq. (5) provides two equations for four unknowns \mathbf{H}_{xx} , \mathbf{H}_{xy} , \mathbf{H}_{yx} , \mathbf{H}_{yy} . To provide four independent equations, alternate shakes about an eccentric rotor position

are conducted on the stator in orthogonal directions (x and y), yielding four equations and four unknowns, given by

$$\begin{bmatrix} F_{xx} - M_s A_{xx} & F_{xy} - M_s A_{xy} \\ F_{yx} - M_s A_{yx} & F_{yy} - M_s A_{yy} \end{bmatrix} = \begin{bmatrix} \mathbf{H}_{xx} & \mathbf{H}_{xy} \\ \mathbf{H}_{yx} & \mathbf{H}_{yy} \end{bmatrix} \begin{bmatrix} D_{xx} & D_{xy} \\ D_{yx} & D_{yy} \end{bmatrix} \quad (7)$$

After solving for the dynamic stiffnesses (\mathbf{H}_{xx} , \mathbf{H}_{xy} , \mathbf{H}_{yx} , \mathbf{H}_{yy}), the 32 separate shake tests are averaged in the frequency domain. For all dynamic test conditions, ten consecutive tests are conducted to evaluate repeatability of the dynamic stiffnesses. Thus, a total of 320 dynamic stiffness coefficients are measured for each frequency (20-220 Hz, at 10 Hz increments).

The variability of each dynamic stiffness is calculated at each frequency. An uncertainty value is obtained for the tests as *two* times the standard deviation of the ten individual dynamic stiffnesses. Also note that an uncertainty value is obtained for each dynamic impedance at all frequencies in the range. Some data points are omitted from each test. These points include 60 Hz and its multiples, which are tainted by electrical noise, and data points near the shaft's rotation synchronous frequency, which also have high uncertainties.

Uncertainty Analysis and Curve Fitting Procedure

Eq. (6) shows that the real part of the dynamic stiffness is a quadratic function of the excitation frequency, whereas the imaginary part is a linear function. If the excitation frequency for the real part of the dynamic stiffness is given a new variable with the relationship, $\Lambda = \Omega^2$, then the quadratic relationship becomes a linear relationship. Therefore, both the real and imaginary parts of the dynamic stiffness can be evaluated using a linear regression. The regression line for the real part gives the seal stiffness (K_{ij}), obtained from the slope, and the added-mass (M_{ij}), obtained from the negative of the slope. Correspondingly, the slope of the regression line for the imaginary part gives

the damping coefficient (C_{ij}). Note that these values are only estimates because the rotordynamic coefficients are extracted from the dynamic stiffness data, rather than directly measured.

The goodness of the rotordynamic coefficients is analyzed using a confidence interval. For each coefficient, a 95% confidence interval is used, meaning that there is 95% probability that the rotordynamic coefficient lies within this interval. Rodriguez [16] defines the formulas for this computation as follows: “The formulas to compute the slope, the intercept and their uncertainties are listed below. Here, the letters x and y refer to a pair of data (x_i, y_j) for the linear regression. They do not refer to the x and y directions as defined in Figure 10.

Number of data pairs, (x_i, y_i)	N	
Regression line equation	$\hat{y} = \beta_0 + \beta_1 x$; \hat{y} denotes the predicted value	
Mean of the x 's	$\bar{x} = \frac{1}{N} \sum_{i=1}^N x_i$	
Mean of the y 's	$\bar{y} = \frac{1}{N} \sum_{i=1}^N y_i$	
Slope	$\beta_1 = \frac{\sum_{i=1}^N y_i x_i - N(\bar{y})(\bar{x})}{\sum_{i=1}^N x_i^2 - N(\bar{x})^2}$	(8a)

Intercept	$\beta_0 = \bar{y} - \beta_1 \bar{x}$	(8b)
-----------	---------------------------------------	------

Mean Square Error, $\hat{\sigma}^2$	$\frac{\sum_{i=1}^N (y_i - \hat{y}_i)^2}{N - 2}$	
S_{xx}	$\sum_{i=1}^N x_i^2 - N \bar{x}^2$	
Uncertainty of the slope, $\Delta\beta_1$	$t \times \sqrt{\frac{\hat{\sigma}^2}{S_{xx}}}$	(8c)

Uncertainty of the
intercept, $\Delta\beta_0$

$$t \times \sqrt{\hat{\sigma}^2 \left(\frac{1}{N} + \frac{\bar{x}^2}{S_{xx}} \right)} \quad (8d)$$

Notice that the uncertainty includes a parameter denoted as t . In general terms, this is a multiplicative factor that depends on the desired probability that the unknown “true” parameter is contained in the interval $\beta_0 \pm \Delta\beta_0$ (or, $\beta_1 \pm \Delta\beta_1$). Obviously, a high probability is desirable, thus it is set to 95%, which yields $t=1.960$. This probability is commonly referred to as “confidence level”.

STATIC PERFORMANCE

This section includes the following static performance data: applied static load, inlet and outlet temperatures, outlet pressures, and flow rates. Each is recorded for the ten consecutive tests at each operating condition of shaft rotational speed, inlet pressure, and eccentricity. For notation purposes, the low inlet oil pressure (24 bars) is denoted as LP; 45 bars, MP; and 70 bars, HP. The complete table of test conditions at which static data is recorded is given above in Table 2. Note that this table corresponds identically to the dynamic data test matrix.

Stator position is recorded in the TS (turbine side) and NTS (non-turbine side) planes in both x and y directions. The average eccentricity is determined by the average of the TS and NTS values. The resulting eccentricity is then determined from the averages in the x and y directions by calculating the resultant. Eqs. (9), (10), and (11) describe this calculation:

$$e_{x_o-ave} = \frac{X_{NTS} + X_{TS}}{2}, \quad e_{y_o-ave} = \frac{Y_{NTS} + Y_{TS}}{2} \quad (9)$$

$$\varepsilon_{x_o} = \frac{e_{x_o-ave}}{C} \quad \varepsilon_{y_o} = \frac{e_{y_o-ave}}{C} \quad (10)$$

and

$$\varepsilon_o = \sqrt{\varepsilon_{x_o}^2 + \varepsilon_{y_o}^2} \quad (11)$$

Figure 11 shows the seal motion relative to the rotor for a groove depth-to-clearance ratio (D_g/C) = 10 and an operating speed of 7000 rpm. The load is applied in the negative y-direction. The locus plot at each pressure shows a drastic movement in the direction normal to the applied load. This result suggests significant seal cross-coupled stiffness.

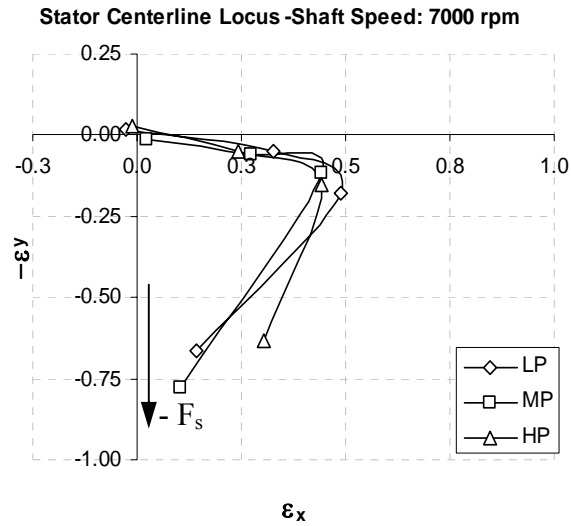


Figure 11. Seal centerline loci plots for three inlet pressures (LP, MP, HP) at an operating speed of 7000 rpm for a $D_g/C = 10$

In addition to eccentricity, attitude angle describes the position of the seal and is characterized by the equation

$$\phi = \tan^{-1} \left(\frac{\varepsilon_{x_o}}{\varepsilon_{y_o}} \right) \frac{180}{\pi} \quad (12)$$

Figure 12 shows the attitude angle versus unit loading for three pressures at 7000 rpm. Attitude angles are large (near 90°) for lower loads. As the seal moves toward the center in the x-direction, Figure 12 shows the attitude angle decreasing toward zero.

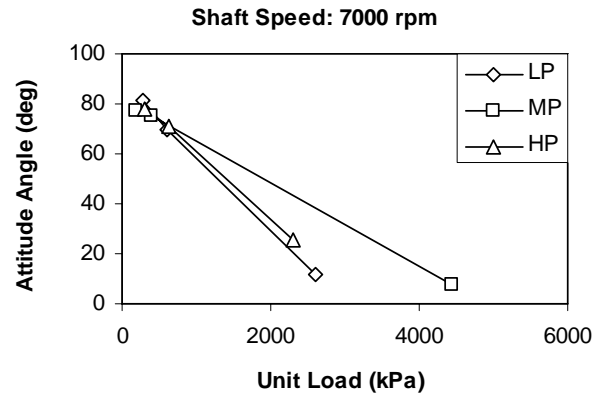


Figure 12. Attitude angle versus unit load for three inlet pressures (LP, MP, HP) at an operating speed of 7000 rpm for a $D_g/C = 10$

Figure 13 depicts the attitude angle versus Sommerfeld number (S). S is defined by

$$S = \frac{\mu_{T_{avg}} NLD}{F_s} \left(\frac{D}{2C} \right)^2, \quad (13)$$

where $\mu_{T_{avg}}$ is oil viscosity at the average of oil inlet and outlet temperatures. Through a comparison between Figure 12 and Figure 13, the attitude angle decreases with load, while increasing with Sommerfeld number; this relationship corresponds to the above equation for S .

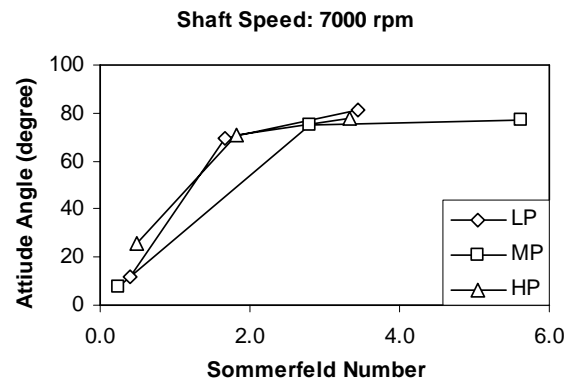


Figure 13. Attitude angle versus Sommerfeld number for three inlet pressures (LP, MP, HP) at an operating speed of 7000 rpm for a $D_g/C = 10$

Seal leakage is an important characteristic for the seals: reducing leakage is the primary reason for implementing them into a rotor-bearing system. Figure 14 shows the seal's leakage rate for a $D_g/C = 10$ versus eccentricity. The leakage increases with (a) inlet pressure and (b) operating speed, as well as a slight increase with increasing eccentricity.

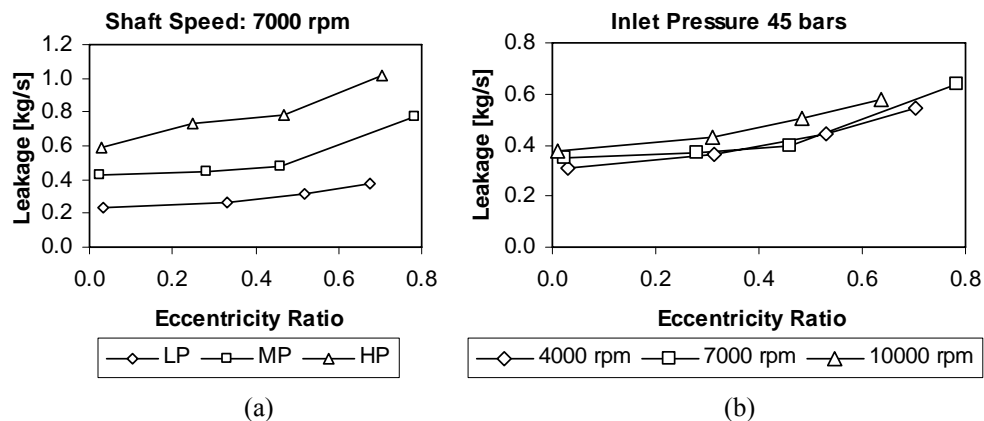


Figure 14. Seal leakage versus eccentricity ratio for (a) 7000 rpm and varying pressures (LP, MP, HP) and (b) 45 bars and varying speeds (4000, 7000, 10000 rpm)

DYNAMIC PERFORMANCE CHARACTERISTICS

Measurement of Baseline

For each test, rotordynamic coefficients are measured for the entire system. To determine the rotordynamic coefficients for the seals, external sources of stiffness must be excluded from the measurements. External sources of stiffness for this system include pitch stabilizers, oil hose connections, and static loader yoke, etc. To account for these additional elements, baseline tests are performed. Test conditions of the baseline test are zero rotor speed, and no supplied oil. All baseline values in Figure 15 for dynamic stiffness are very small. These values will be subtracted from dynamic stiffnesses of seal tests to analyze only seal dynamic stiffness. Note that the baseline and the tests already account for the direct mass of the stator (Eq. (4)). Their magnitude will be further analyzed in the Seal Dynamic Stiffness section below.

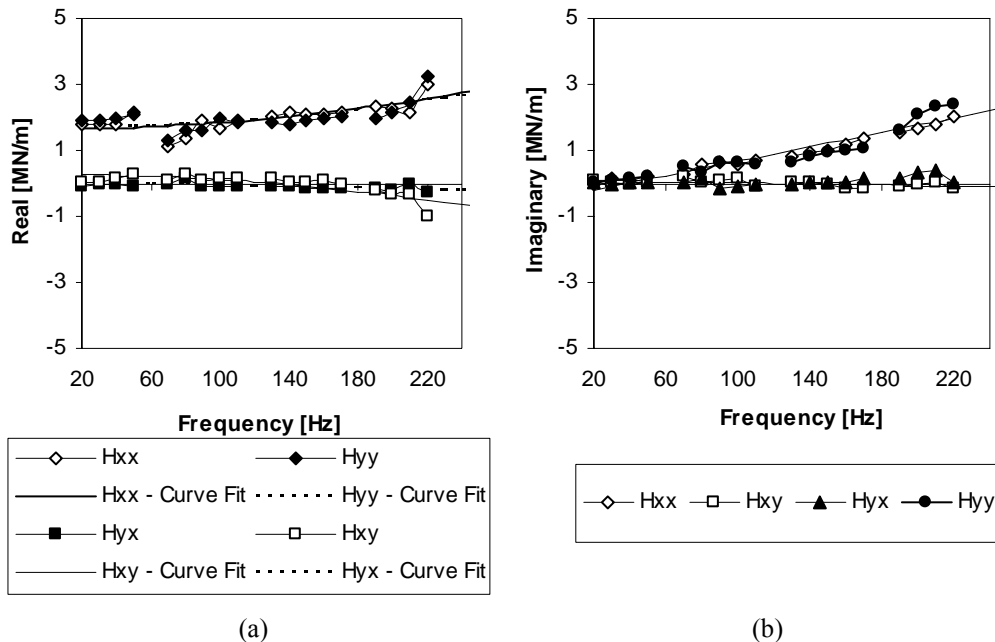


Figure 15. Baseline dynamic stiffness

Seal Dynamic Stiffness

This section provides example dynamic stiffness coefficients for the seal with a D_g/C of 5, rotor speed of 10000 rpm, inlet pressure of 70 bars, and an eccentricity of 0.5. Figure 16 shows the real part of the dynamic stiffness, while Figure 17 shows the imaginary part. Each figure also includes the corresponding baseline dynamic stiffness to show that the baseline is minimal in comparison to test condition values. As previously mentioned, the dynamic stiffness values include error bars that represent the degree of variability in the data, while uncertainty defined in rotordynamic coefficients is obtained from the confidence interval of the curve fit (Eqs. 15, 16, and 17).

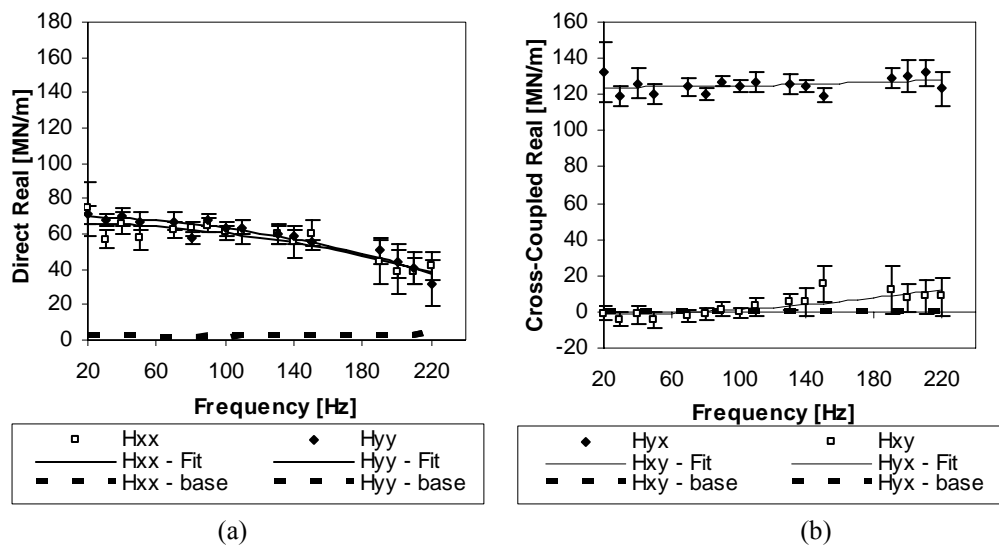


Figure 16. Real direct and cross-coupled dynamic stiffness at 10000 rpm, 70 bars, and ϵ of 0.5

As described in an earlier section, stiffness and added-mass coefficients are obtained from the least-squares linear regression of the dynamic stiffness in the form

$$\text{Re}(\mathbf{H}_{ij}) = K_{ij} - M_{ij} \Omega^2 \quad (14)$$

Thus, the stiffness coefficients of the seal corresponding to dynamic stiffness data viewed in Figure 16 and obtained by use of Eqs. 8(a) and 8(c) are

$$\begin{aligned} M_{xx} &= 14.5 \pm 3.6 \text{ kg} & M_{yy} &= 16.8 \pm 2.4 \text{ kg} \\ K_{xx} &= 66.3 \pm 3.4 \text{ MN/m} & K_{yy} &= 69.9 \pm 2.2 \text{ MN/m} \end{aligned} \quad (15)$$

and

$$\begin{aligned} M_{xy} &= -7.4 \pm 2.9 \text{ kg} & M_{yx} &= -2.1 \pm 3.1 \text{ kg} \\ K_{xy} &= -1.8 \pm 2.7 \text{ MN/m} & K_{yx} &= 123.9 \pm 2.9 \text{ MN/m} \end{aligned} \quad (16)$$

Figure 16 shows frequency dependency for direct real stiffness in both the x and y directions; the direct added-mass coefficients reflect this frequency dependency.

Figure 17 shows the direct and cross-coupled imaginary parts of dynamic stiffness. Again, the baseline dynamic stiffnesses are included in the plots to show their minimal impact on seal dynamic stiffness. The direct imaginary dynamic stiffness is significantly larger than the cross-coupled.

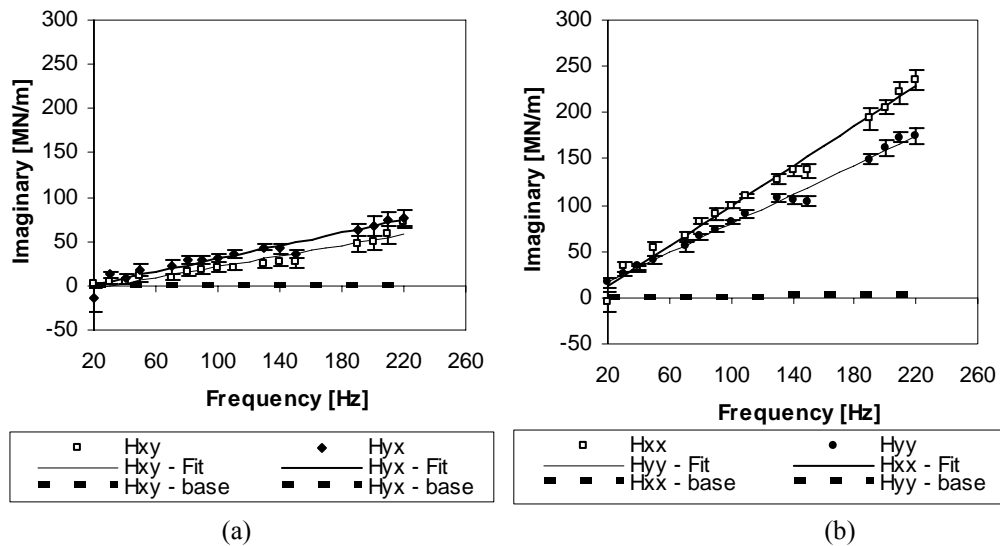


Figure 17. Imaginary direct dynamic stiffness at 10000 rpm, 70 bars, and ϵ of 0.5

The damping coefficients are obtained from the slope of the imaginary part of the dynamic stiffness depicted in Figure 17. Values obtained for damping are

$$\begin{aligned} C_{xx} &= 172.3 \pm 9.5 \text{ kN-s/m} & C_{xy} &= 48.1 \pm 7.5 \text{ kN-s/m} \\ C_{yy} &= 125.3 \pm 6.2 \text{ kN-s/m} & C_{yx} &= 58.5 \pm 7.7 \text{ kN-s/m} \end{aligned} \quad (17)$$

EXPERIMENTAL RESULTS AND PREDICTIONS

Experimental results are described in this section in two ways. First, a comparison of the four test seals is conducted to determine how much the rotordynamic coefficients and seal leakage are affected by increasing the groove depth on the seal. And second, the grooved seals are compared with a theoretical model (XLTRC² – XLLubeGT)¹ to determine at what groove depth the experimental data coincides, and therefore becomes effective. The purpose for separating the comparisons in this manner is XLLubeGT uses a synchronous analysis. For example, if the operating speed is 4000 rpm, the code predicts stiffness and damping coefficients at the corresponding frequency (116 Hz). Therefore, to compare to XLLubeGT, experimental dynamic stiffness data at the synchronous frequency, obtained from the curve-fit, is used. While on the other hand, experimental data among the various test seals can be compared using the rotordynamic coefficients obtained over the entire frequency range.

Influence of Groove Depth

The influence of groove depth on dynamic characteristics of an oil seal can be analyzed through a direct comparison of the seals' rotordynamic coefficients. San Andrés [17] describe the decrease in rotordynamic coefficients from a 1-land seal and a 2-land seal as follows:

$$K_{xx}(1 \text{ land})=2K_{xx}(2 \text{ lands}) \quad K_{yy}(1 \text{ land})=2K_{yy}(2 \text{ lands})$$

$$K_{xy}(1 \text{ land})=4K_{xy}(2 \text{ lands}) \quad K_{yx}(1 \text{ land})=4K_{yx}(2 \text{ lands})$$

$$C_{xx}(1 \text{ land})=4C_{xx}(2 \text{ lands}) \quad C_{yy}(1 \text{ land})=4C_{yy}(2 \text{ lands})$$

Therefore, this section compares the seals with different grooves and analyzes the amount that each of these coefficients is decreased. For each plot in this sub-section, a

¹ Developed by Semanate and San Andrés [2] and is part of the XLTRC² Rotordynamics Software Suite developed at the Texas A&M Turbomachinery Laboratory.

seal is labeled by its D_g/C ratio (0, 5, 10, 15). Figure 18 represents the trend of K_{xy} with eccentricity for the three inlet oil pressures. The relationship between the seals with various groove depths varies little with inlet oil pressure. Hence, all results for stiffness coefficients will be presented for the three rotor speeds and varying eccentricities, with one oil inlet pressure (70 bars).

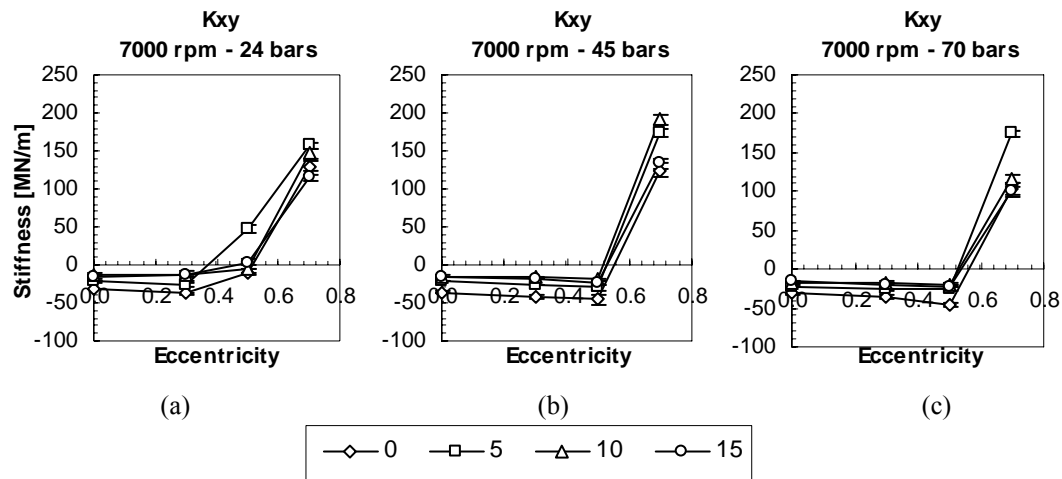


Figure 18. Cross-coupled stiffness (K_{xy}) versus eccentricity for all test seals and three inlet oil pressures

At all speeds, the direct stiffness in the x-direction is nearly zero for operating eccentricities of 0, and 0.3, while beginning to increase at 0.5 eccentricity only for 7000 rpm and 10000 rpm, as shown in Figure 19. Each plot shows a steady decrease in stiffness as the groove depth increases. In comparing the smooth seal (0) with the largest groove depth seal (15), the stiffness in the x-direction for the grooved seal is, on average, 27.7% of the stiffness of the smooth seal at 0.5 eccentricity and 49.4% at 0.7 eccentricity. Therefore, the seal with the largest groove depth succeeds in decreasing the direct stiffness in the x-direction by half.

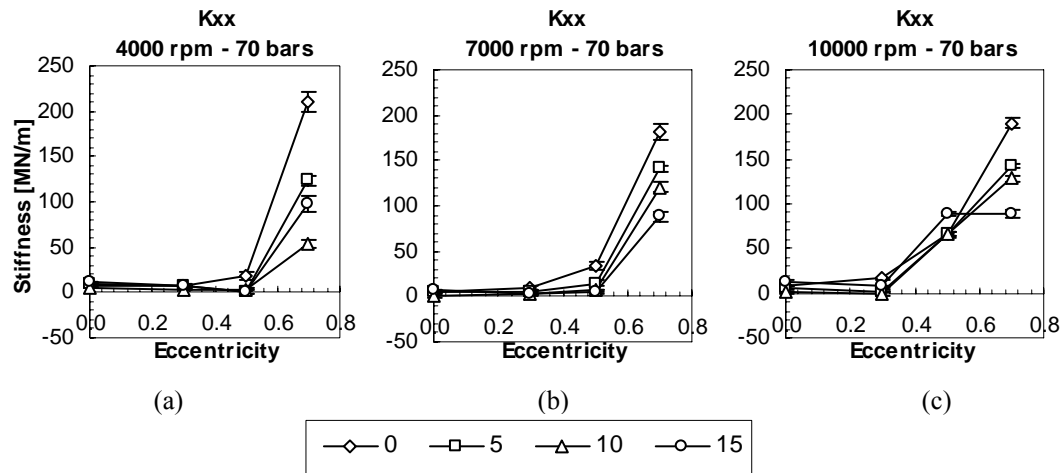


Figure 19. Direct stiffness in the x-direction versus eccentricity for each rotor speed

Figure 20 presents a comparison of groove depth for direct stiffness in the y-direction with increasing eccentricities.

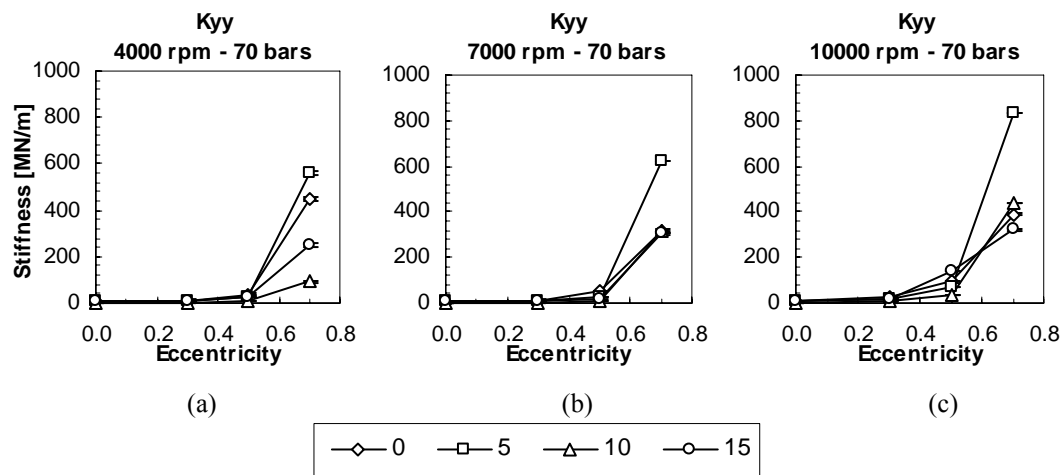


Figure 20. Direct stiffness in the y-direction versus eccentricity for each rotor speed

Trends with eccentricity in Figure 20 correspond to those of Figure 19, though stiffness in the y-direction remains nearly zero for 0.5 eccentricity as well. In again comparing the smooth seal (0) with the largest groove depth seal (15), the stiffness in the y-direction for the grooved seal is, on average, 81.9% of the stiffness of the smooth seal at

0.7 eccentricity. So it is clear that even the largest groove depth is not deep enough to match predictions ($1\text{-land} = 2 * 2\text{-land}$).

The cross-coupled stiffness coefficients (K_{xy} and K_{yx}) are analyzed in the same way and have similar trends with eccentricity as with direct stiffness terms. The difference in K_{xy} between the smooth seal and the seal with the largest groove depth is much larger at 4000 rpm (Figure 21 (a)): at 4000 rpm the grooved seal ($D_g/C=15$) is 47% of the stiffness of the smooth seal; 7000 rpm, 98.7%; 10000 rpm, 79.8%. Therefore, the largest groove depth still is not large enough to decrease K_{xy} by the code-predicted-75%. The difference in K_{yx} remains the same among different rotor speeds, but with a value only 51.9% of the smooth seal, the groove is clearly not deep enough to create the desired effect (25%).

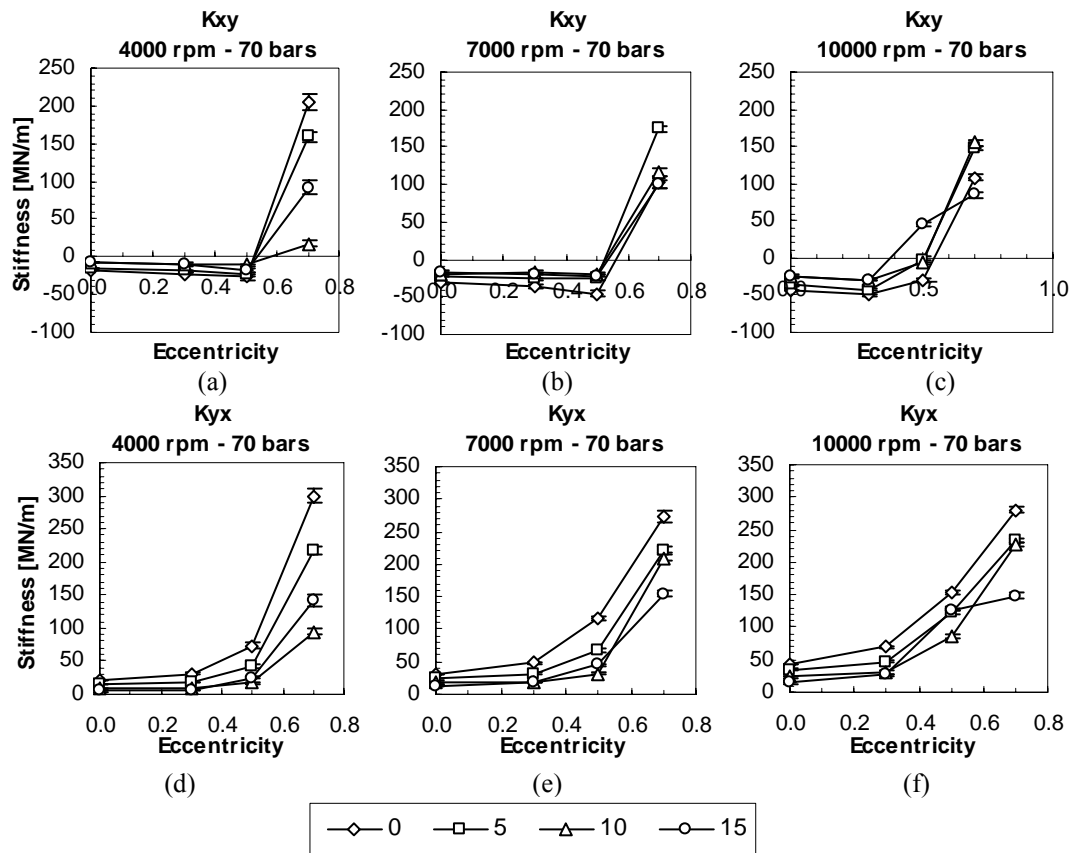


Figure 21. Cross-coupled stiffness (K_{xy} and K_{yx}) versus eccentricity for each rotor speed

Comparison of damping among the test seals with various groove depths is done in the same fashion as that of the stiffness comparison above. Figure 22 displays the trend that damping varies little with oil inlet pressure. Though Figure 22 only depicts direct damping in the y-direction, all damping coefficients have this same trend with inlet pressure. Therefore, all results for damping coefficients will be presented for the three rotor speeds and varying eccentricities, with one oil inlet pressure (70 bars).

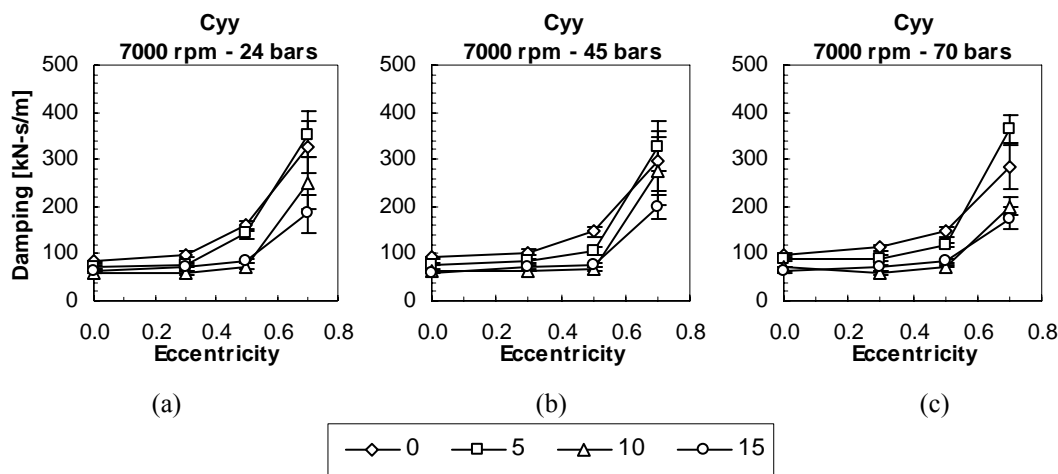


Figure 22. Direct damping in the y-direction vs. eccentricity at 7000 rpm for oil inlet pressures of (a) 24 bars (b) 45 bars (c) 70 bars

Figure 23 details the direct damping in the x-direction (C_{xx}) versus eccentricity for speeds of (a) 4000 rpm, (b) 7000 rpm and (c) 10000 rpm. The difference in damping at 0.7 eccentricity between the smooth seal and the seal with the largest groove depth is about 40%, though the predicted reduction is 75%. Direct damping in the x-direction has a larger difference at 0.5 eccentricity, though still not large enough to create the desired effect. Figure 23 also illustrates that, for the deeper grooved seals (D_g/C), direct damping does not change much with rotor speed. Direct damping in the y-direction (C_{yy}) for each rotor speed is depicted in Figure 24. Comparing the smooth seal (0) with the largest groove depth seal (15), the stiffness in the y-direction for the grooved seal is, on average, 59.8% of the stiffness of the smooth seal at 0.7 eccentricity (predicted: 25%). Unlike

C_{xx} , C_{yy} is largest at 0.7 eccentricity. Overall, the seal with the largest groove depth does not produce the predicted 75% reduction in direct damping.

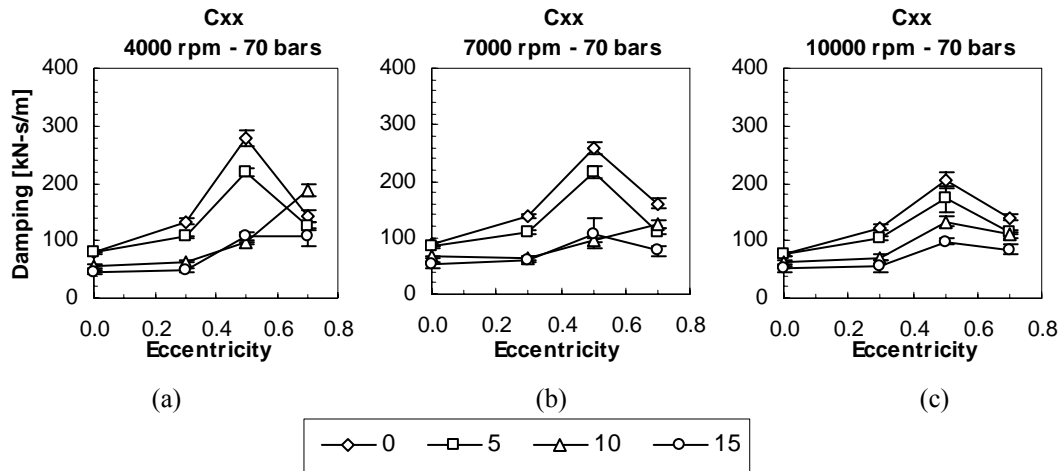


Figure 23. Direct damping in the x-direction versus eccentricity for each rotor speed

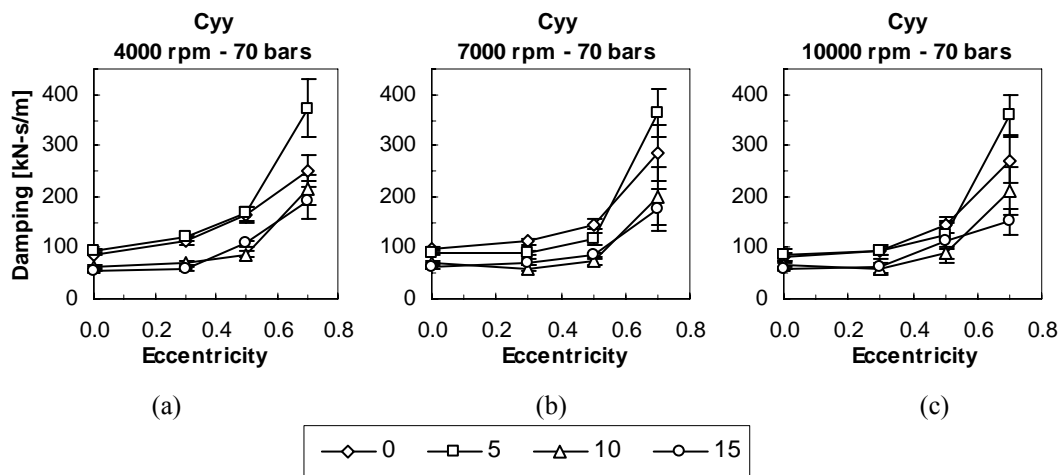


Figure 24. Direct damping in the y-direction versus eccentricity for each rotor speed

XLLubeGT predicts zero cross-coupled damping. However, Figure 25 shows that there is significant cross-coupled damping in experimental results, particularly at high eccentricities. C_{xy} increases with eccentricity, while C_{yx} increases to 0.5 eccentricity then

nears zero as eccentricity increases to 0.7. Additionally, cross-coupled damping does not vary much with rotor speed.

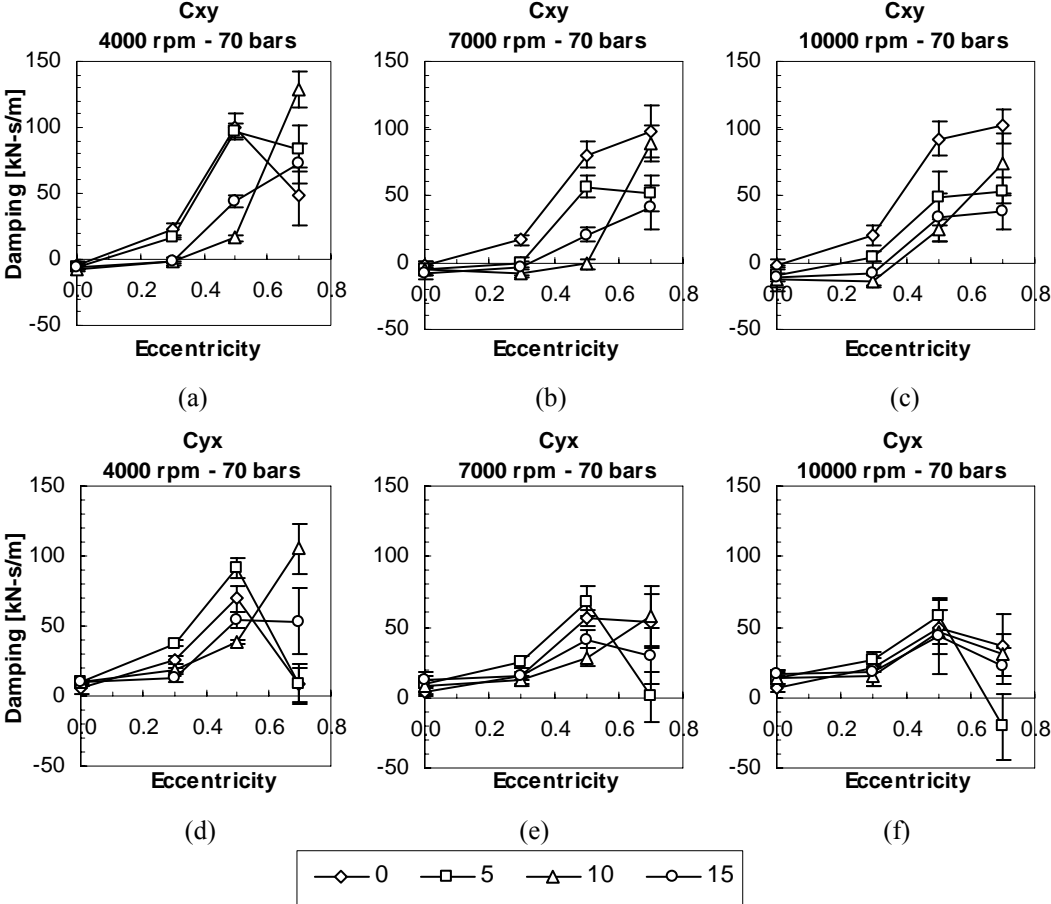


Figure 25. Cross-coupled damping (C_{xy} and C_{yx}) vs. eccentricity for each rotor speed

In addition to stiffness and damping coefficients, added mass coefficients are compared among the seals. However, only direct added mass coefficients are compared: cross-coupled added mass coefficients are nearly zero for all conditions and grooved seals (the smooth seal has a cross-coupled added mass at 0.7 eccentricity of about -20 kg). At the lowest inlet pressure for each speed, and at the lowest rotor speed for each inlet pressure, Figure 26 shows that only the smooth seal returns to zero added mass at 0.5 eccentricity, while all other test conditions and grooved seals show a decrease at 0.7 eccentricity.

Added mass in the y-direction, for nearly all test conditions and groove depths, shows a constant added mass through the range of eccentricities. For most test conditions, the added mass decreases with a decrease in groove depth. The seal with the largest groove depth has an average added-mass of 30 kg, and the smooth seal has an average added mass of 11 kg. Extremely large M_{yy} values correspond to extremely large values of K_{yy} . For example, in Figure 27(i), the added mass value for the $D_g/C=5$ is 112 kg, and the corresponding direct stiffness value is 830 MN/m (see Figure 20(c)).

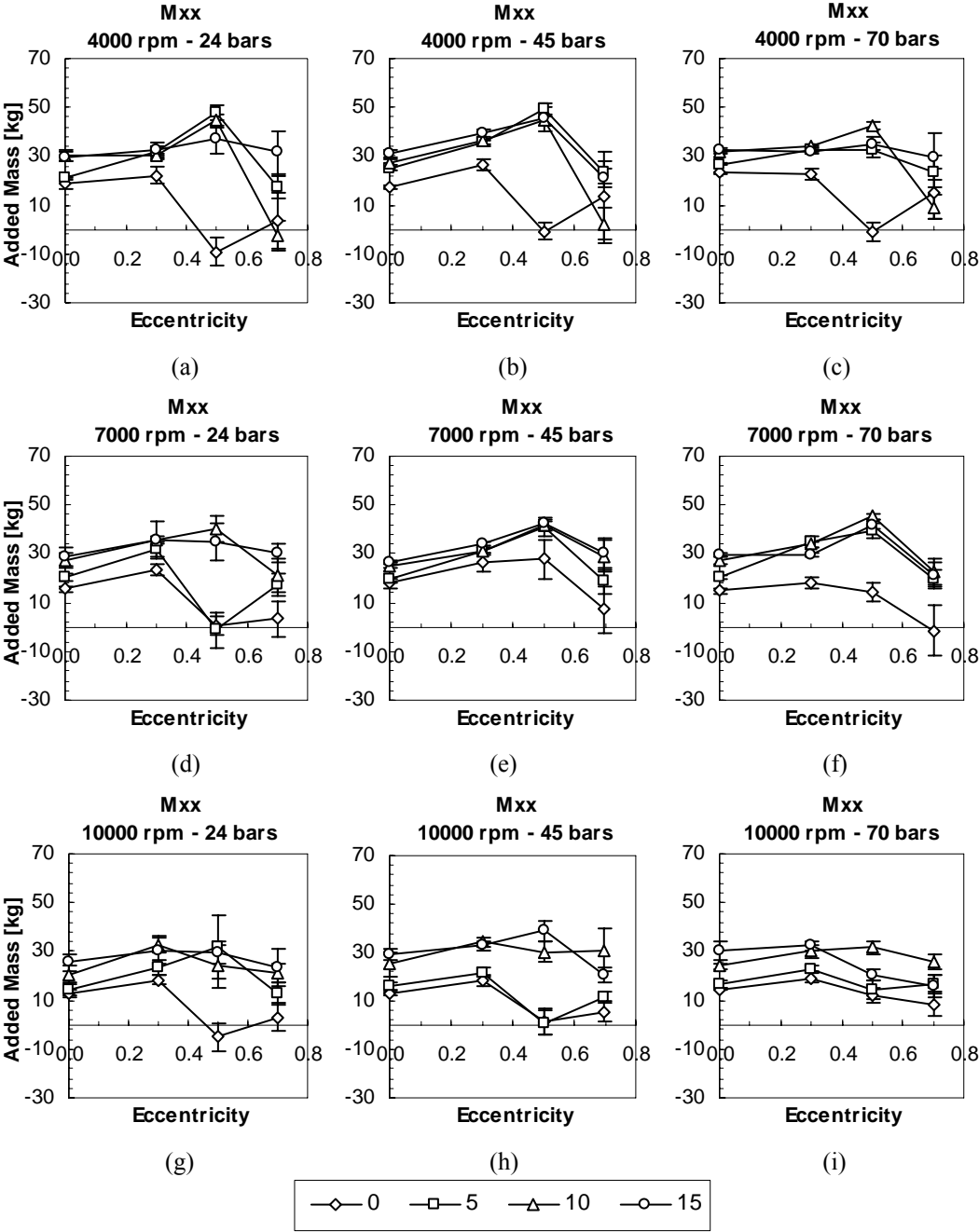


Figure 26. Direct added mass in the x-direction for all test rotor speeds and oil inlet pressures

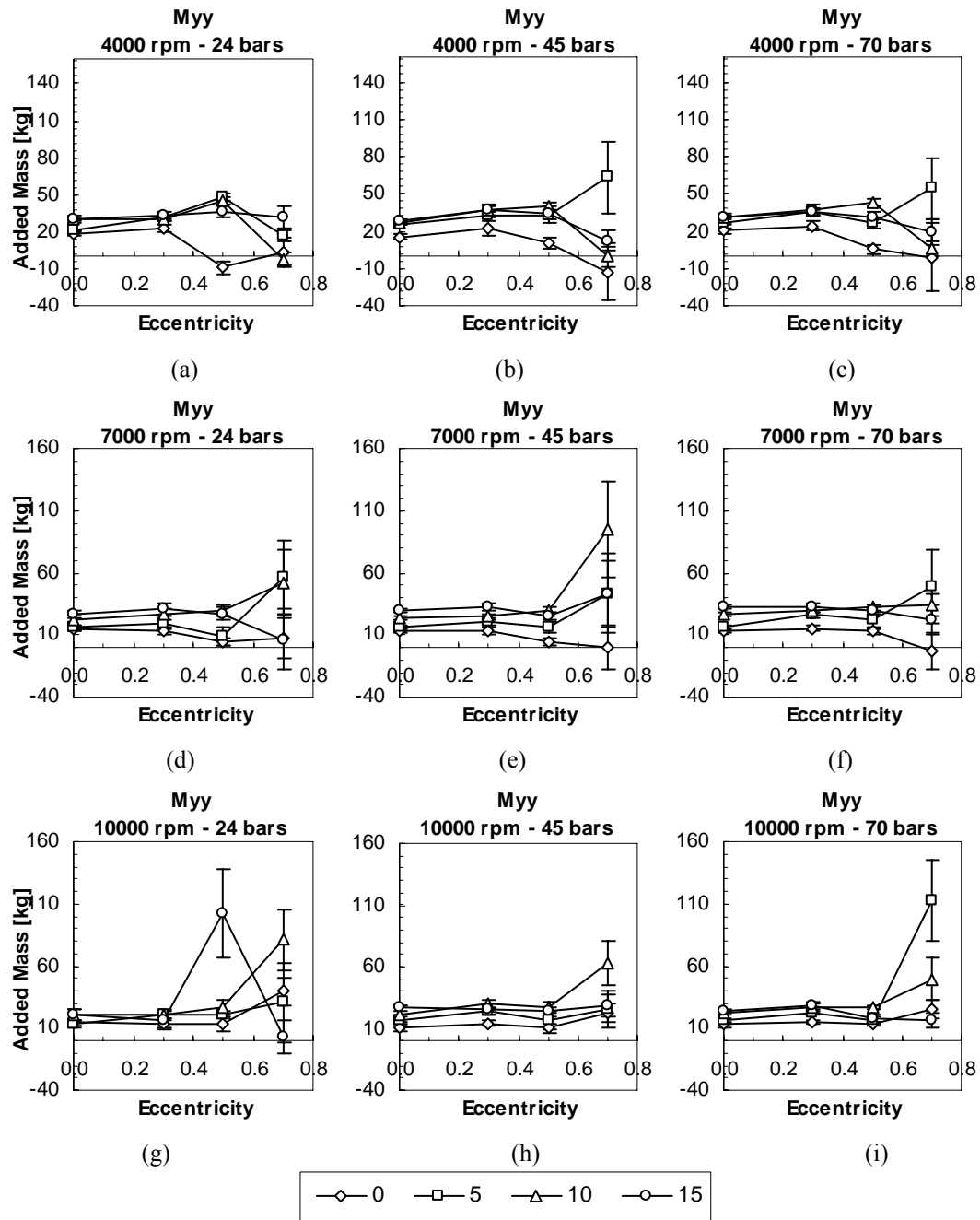


Figure 27. Direct added mass in the y-direction for all test rotor speeds and oil inlet pressures

Added mass from a seal has been an ongoing study for all seal tests conducted on the test rig used for this investigation. To date, no one has explained the large inertial terms obtained in seal data from this test rig. XLLubeGT predicts zero added mass; it is based on the Reynolds equation, which neglects inertial effects. However, Figure 26 and Figure 27 contradict this assumption (added mass values : 30 kg). Lund [18] uses Eq. (18) to calculate inertial terms for journal bearings with small length-to-diameter ratios ($L/D \ll 0.5$). This equation results in an added mass value for the test seals of 2.84 kg, which is much smaller than measurements.

$$M = \frac{\rho \cdot \pi \cdot R \cdot L^3}{10 \cdot C} \quad (18)$$

XLTRC² – XLLubeGT

XLLubeGT is a computer code created to analyze the rotordynamic coefficients of laminar oil bushing seals with smooth and circumferentially grooved geometries. The code is based on a Reynold's equation model plus the energy equation for temperature predictions. The model assumes that a groove in a seal is large enough to create separate lands within the seals, yielding zero groove pressure perturbations (groove depth is not an input of this code). Based on this assumption, seals with grooves are predicted to have considerably lower stiffness and damping coefficients and load capacity in comparison to a smooth seal. XLLubeGT also operates on the assumption that the groove does not influence inertial terms, though experimental results show a 20 kg difference between the smooth and grooved seals. Table 3 shows the maximum Reynolds Number for different rotor speeds; the maximum Reynolds Number is a magnitude of the axial and circumferential Reynolds Numbers. All values are considerably less than the maximum Reynolds Number (2000) for operation in the laminar flow regime.

Table 3. Maximum Reynolds numbers for different rotor speeds

Rotor Speed (rpm)	4000	7000	10000
Max. Reynolds Number	169.2	283.5	402.5
Axial ($\rho * W_o C / \mu$)	52.7	34.6	18.6
Circumferential ($2 * \rho C \omega r / \mu$)	160.8	281.4	402.0

Input values into XLLubeGT that remain constant through the entire series of test conditions are seal material (660 Brg Bronze) and seal geometry. Lubricant properties including viscosity and density vary with the input temperature, which slightly varies with each test condition. Also, each test condition is entered into the code: shaft speed, inlet and outlet pressure, and eccentricity (x and y-directions). Test conditions used in XLLubeGT analysis correspond to those used for experiments (Table 2). Results of XLLubeGT pertinent to this analysis include stiffness and damping coefficients, and seal leakage. Note that the “cold” clearance is used for XLLubeGT predictions in this section. The “cold” clearance was measured prior to test rig assembly, and was verified by a bump test prior to testing. Actual clearance predictions are discussed in a later section.

Prior to comparing experimental dynamic data to XLLubeGT, an incongruity in coordinate reference frames must be resolved. Figure 28 shows the coordinate frames for (a) the test rig and (b) XLLubeGT.

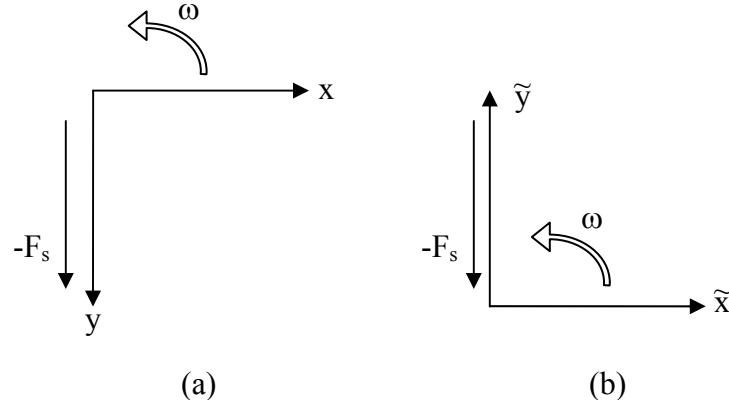


Figure 28. Coordinate frame for (a) experiments and (b) XLLubeGT

Based on the coordinate frames in Figure 28, Eqs. (20) and (21) describe the reaction force equations for experimental and theory, respectively:

$$-\begin{bmatrix} f_{sx} \\ f_{sy} \end{bmatrix} = \begin{bmatrix} K_{xx} & K_{xy} \\ K_{yx} & K_{yy} \end{bmatrix} \begin{bmatrix} \Delta x \\ \Delta y \end{bmatrix} + \begin{bmatrix} C_{xx} & C_{xy} \\ C_{yy} & C_{yy} \end{bmatrix} \begin{bmatrix} \Delta \dot{x} \\ \Delta \dot{y} \end{bmatrix} + \begin{bmatrix} M_{xx} & M_{xy} \\ M_{yx} & M_{yy} \end{bmatrix} \begin{bmatrix} \Delta \ddot{x} \\ \Delta \ddot{y} \end{bmatrix} \quad (19)$$

$$-\begin{bmatrix} \tilde{f}_{sx} \\ \tilde{f}_{sy} \end{bmatrix} = \begin{bmatrix} \tilde{K}_{xx} & \tilde{K}_{xy} \\ \tilde{K}_{yx} & \tilde{K}_{yy} \end{bmatrix} \begin{bmatrix} \Delta \tilde{x} \\ \Delta \tilde{y} \end{bmatrix} + \begin{bmatrix} \tilde{C}_{xx} & \tilde{C}_{xy} \\ \tilde{C}_{yy} & \tilde{C}_{yy} \end{bmatrix} \begin{bmatrix} \Delta \dot{\tilde{x}} \\ \Delta \dot{\tilde{y}} \end{bmatrix} + \begin{bmatrix} \tilde{M}_{xx} & \tilde{M}_{xy} \\ \tilde{M}_{yx} & \tilde{M}_{yy} \end{bmatrix} \begin{bmatrix} \Delta \ddot{\tilde{x}} \\ \Delta \ddot{\tilde{y}} \end{bmatrix}, \quad (20)$$

where

$$\begin{bmatrix} f_{sx} \\ f_{sy} \end{bmatrix} = \begin{bmatrix} \tilde{f}_{sx} \\ -\tilde{f}_{sy} \end{bmatrix} \quad \text{and} \quad \begin{bmatrix} x \\ y \end{bmatrix} = \begin{bmatrix} 1 & 0 \\ 0 & -1 \end{bmatrix} \begin{bmatrix} \tilde{x} \\ \tilde{y} \end{bmatrix} \quad (21)$$

Because XLLubeGT computes zero added-mass coefficients, from this point forward, comparisons to theory only consider stiffness and damping coefficients. Substituting Eq. (21) into Eq. (19) converts the rotordynamic coefficients of the code into the coordinate frame of the test rig, giving

$$\begin{bmatrix} \tilde{f}_{sx} \\ \tilde{f}_{sy} \end{bmatrix} = \begin{bmatrix} K_{xx} & -K_{xy} \\ -K_{yx} & K_{yy} \end{bmatrix} \begin{bmatrix} \Delta \tilde{x} \\ \Delta \tilde{y} \end{bmatrix} + \begin{bmatrix} C_{xx} & -C_{xy} \\ -C_{yy} & C_{yy} \end{bmatrix} \begin{bmatrix} \Delta \dot{\tilde{x}} \\ \Delta \dot{\tilde{y}} \end{bmatrix} \quad (22)$$

Thus, the rotordynamic coefficients of the experiments are compared to those of XLLubeGT as follows:

$$\begin{aligned}
 K_{xx} &= K_{\tilde{x}\tilde{x}} , K_{xy} = -K_{\tilde{x}\tilde{y}} , K_{yx} = -K_{\tilde{y}\tilde{x}} , K_{yy} = K_{\tilde{y}\tilde{y}} \\
 C_{xx} &= C_{\tilde{x}\tilde{x}} , C_{xy} = -C_{\tilde{x}\tilde{y}} , C_{yx} = -C_{\tilde{y}\tilde{x}} , C_{yy} = C_{\tilde{y}\tilde{y}}
 \end{aligned}
 \tag{23}$$

With the rotordynamic coefficient conversion completed, it is now possible to compare the test seals with XLLubeGT. The comparison can primarily be reduced to one inlet oil pressure because both the code and the experimental stiffness and damping coefficients vary little with inlet oil pressure. Figure 29 describes this fact using $D_g/C = 15$, for only direct terms, though cross-coupled terms reflect the same trend. Thus, further analysis will depict data at one oil inlet pressure. A zoomed in view of rotordynamic coefficients at lower eccentricities can be found in the appendix.

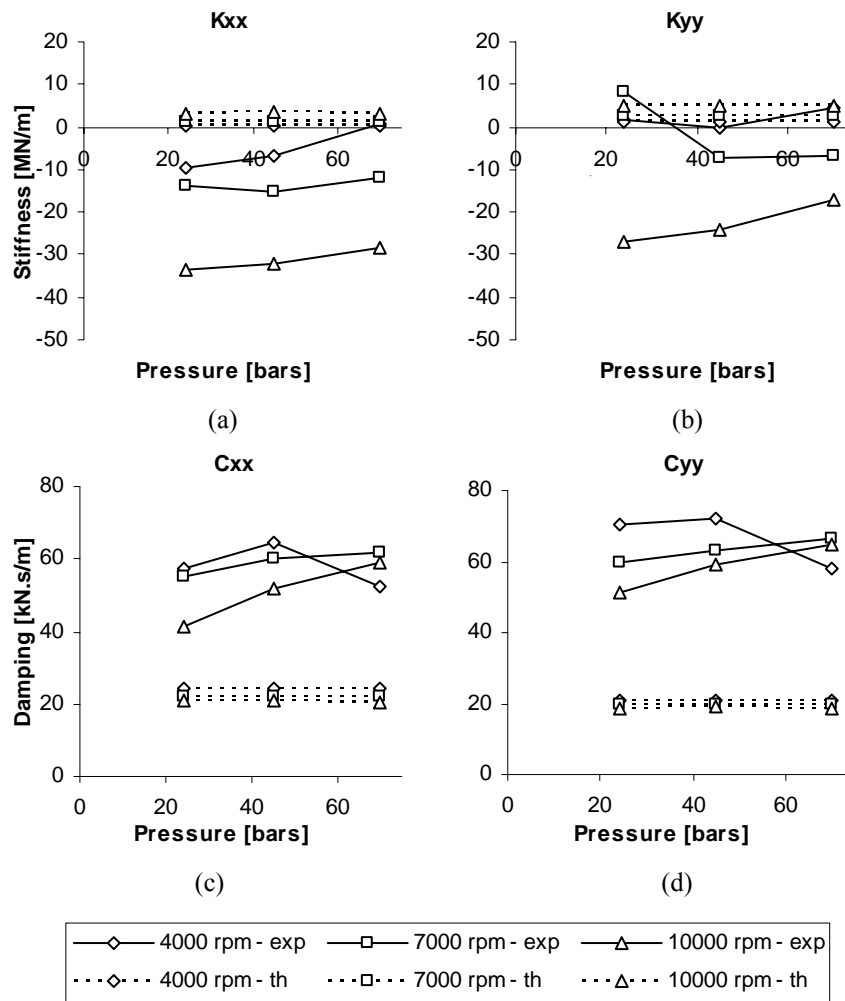


Figure 29. Stiffness and damping coefficients versus oil inlet pressure at $\varepsilon = 0.3$: experimental ($D_g/C = 15$) vs. theory

Figure 30 shows the direct and cross-coupled stiffness coefficients versus eccentricity for the highest test rotor speed (10000 rpm) and the highest test inlet oil pressure (70 bars); all test seals are included, denoted by their D_g/C ratio (0, 5, 10, 15). Figure 30 (a) and (b) show that XLLubeGT predicts zero direct stiffness at all eccentricities. Conversely, experimental results show an increase in direct stiffness at largely eccentric positions, significantly more so in the y-direction. The larger value in the y-direction is expected because it is the direction of the applied static load. It also shows that XLLubeGT matches well with cross-coupled coefficients for eccentricities of

0 and 0.3. However, XLLubeGT under-predicts direct and cross-coupled stiffness coefficients at large eccentricities.

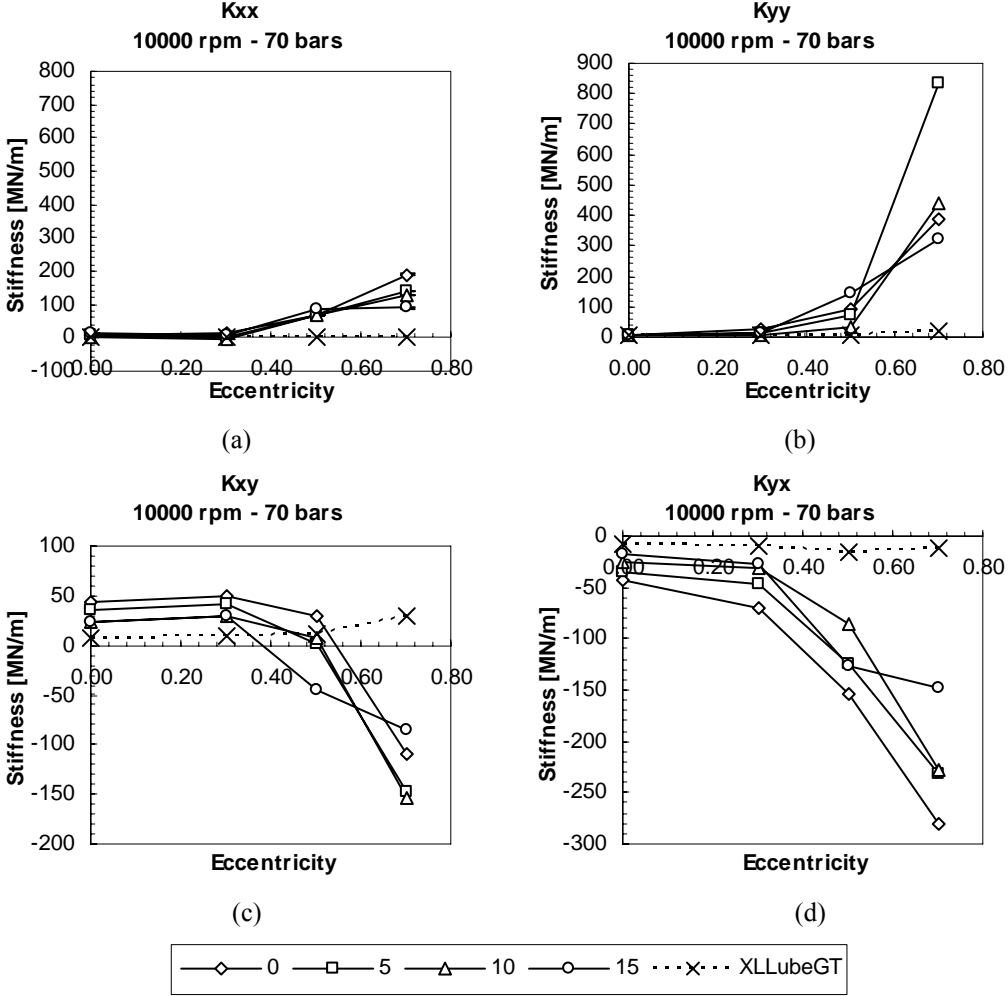


Figure 30. Direct and cross-coupled stiffness coefficients (a) K_{xx} (b) K_{yy} (c) K_{xy} (d) K_{yx} versus eccentricity (0, 0.3, 0.5, 0.7)

As shown in Figure 31, the experimental damping coefficients have the same trend as predictions. As eccentricity increases, C_{xx} slightly increases with a jump at 0.5 eccentricity. Also, C_{yy} remains nearly constant with a sharp increase at 0.7 eccentricity. XLLubeGT predicts nearly zero cross-coupled damping, while experimental data shows larger values, with an increase at 0.5 eccentricity. Regardless, even the test seal with the

largest groove depth does not have damping coefficients that are low enough to correspond to XLLubeGT over the entire eccentricity range.

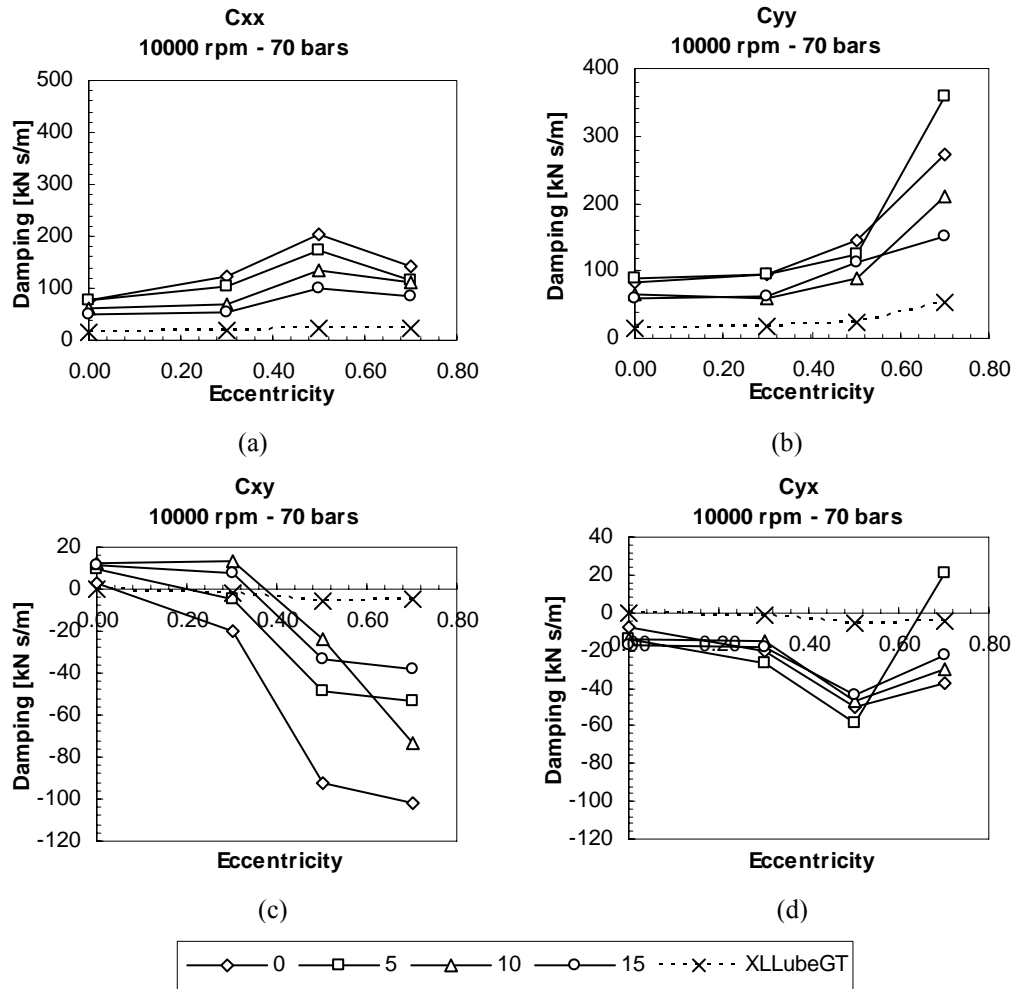


Figure 31. Direct and cross-coupled damping coefficients (a) C_{xx} (b) C_{yy} (c) C_{xy} (d) C_{yx} versus eccentricity (0, 0.3, 0.5, 0.7)

Seal Leakage

Leakage is calculated from XLLubeGT by the product of the volumetric flow rate and the density. Figure 32 shows the leakage rate of the seals as a function of

eccentricity. All trends seen in Figure 32 are consistent for each test condition of rotor speed and inlet oil pressure. Figure 32 shows that there is little difference between leakage rates of XLLubeGT and experimental data. In Figure 32, there is almost no difference between leakage rates of the experimental data with different groove depths. This is the desired effect: though groove depth changes among the seals, seal clearance remains the same, producing equal leakage rates. Overall, it is determined that XLLubeGT accurately predicts leakage rate.

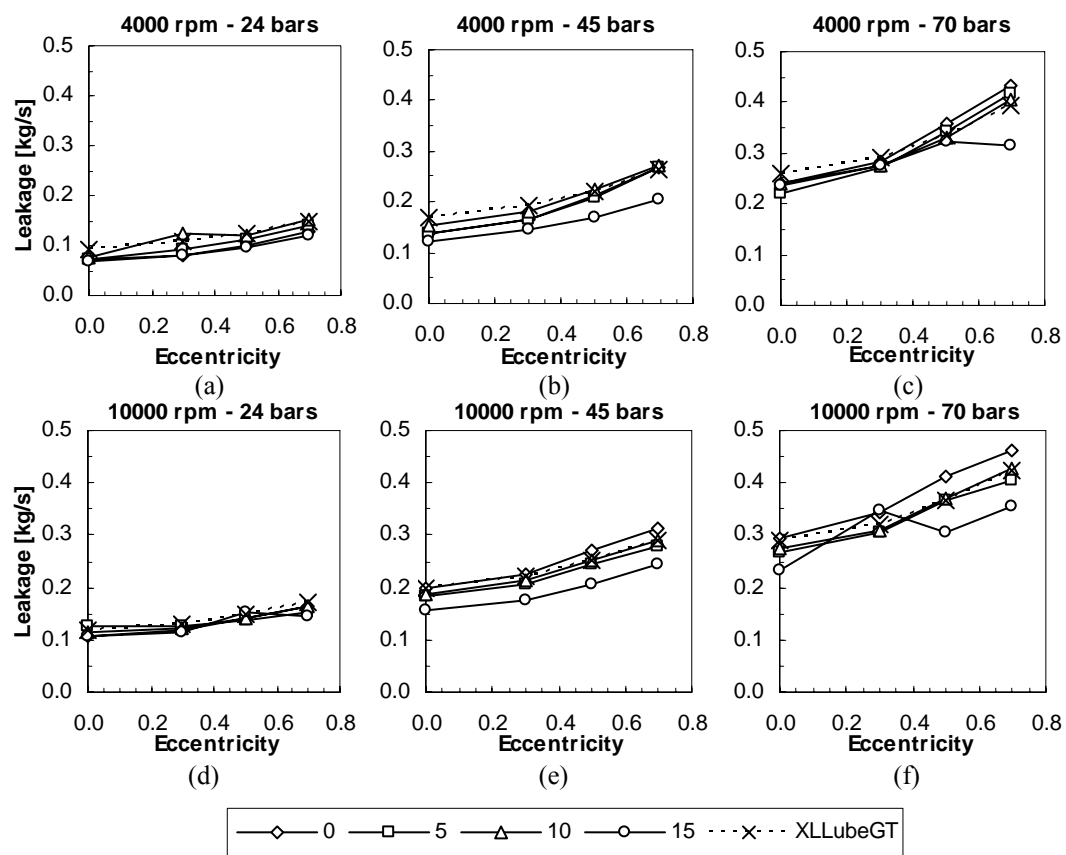


Figure 32. Leakage versus eccentricity for all test speeds and oil inlet pressures

Whirl Frequency Ratio (*WFR*)

The whirl frequency ratio (*WFR*) is the ratio between the rotor precessional frequency and the onset speed of instability (ω_s). It is a parameter used to evaluate stability. As the *WFR* increases, ω_s decreases, indicating a less stable system. For a centered seal, the *WFR* is 0.50 [17], which is the same as that of an unloaded plain journal bearing. The *WFR* is defined by the equation

$$WFR^2 = \left(\frac{\Omega}{\omega_s} \right)^2 = \frac{(K_{eq} - K_{xx}) \cdot (K_{eq} - K_{yy}) - (K_{xy} \cdot K_{yx})}{\omega^2 \cdot (C_{xx} \cdot C_{yy} - C_{xy} \cdot C_{yx})} \quad (24)$$

$$\text{where } K_{eq} = \frac{K_{xx} \cdot C_{yy} + K_{yy} \cdot C_{xx} - K_{xy} \cdot C_{yx} - K_{yx} \cdot C_{xy}}{C_{xx} + C_{yy}}$$

XLLubeGT predicts *WFR* values near 0.5 over the entire frequency range (Figure 33). Experimental results show a sharp drop in *WFR* from 0.5 to 0.7 eccentricity, a similar trend to plain journal bearings. An average *WFR* of 0.4 at low eccentricities proves a quite stable system, and this stability increases with rotor speed. XLLubeGT predicts a decrease at 0.7 eccentricity, but over predicts the *WFR* as a whole. Also, XLLubeGT doesn't predict a *WFR* of zero until nearly 0.8 eccentricity, which is beyond the conditions tested.

Eq. (24) for *WFR* neglects fluid inertia, though fluid inertia is significant in test results. However, the cross-coupled added mass terms obtained from experiments have uncertainties the same order of magnitude as the actual values. Therefore, these values must be eliminated from the *WFR* calculations that consider fluid inertia. After eliminating cross-coupled added mass terms, the *WFR* calculations reduce back to Eq. (24).

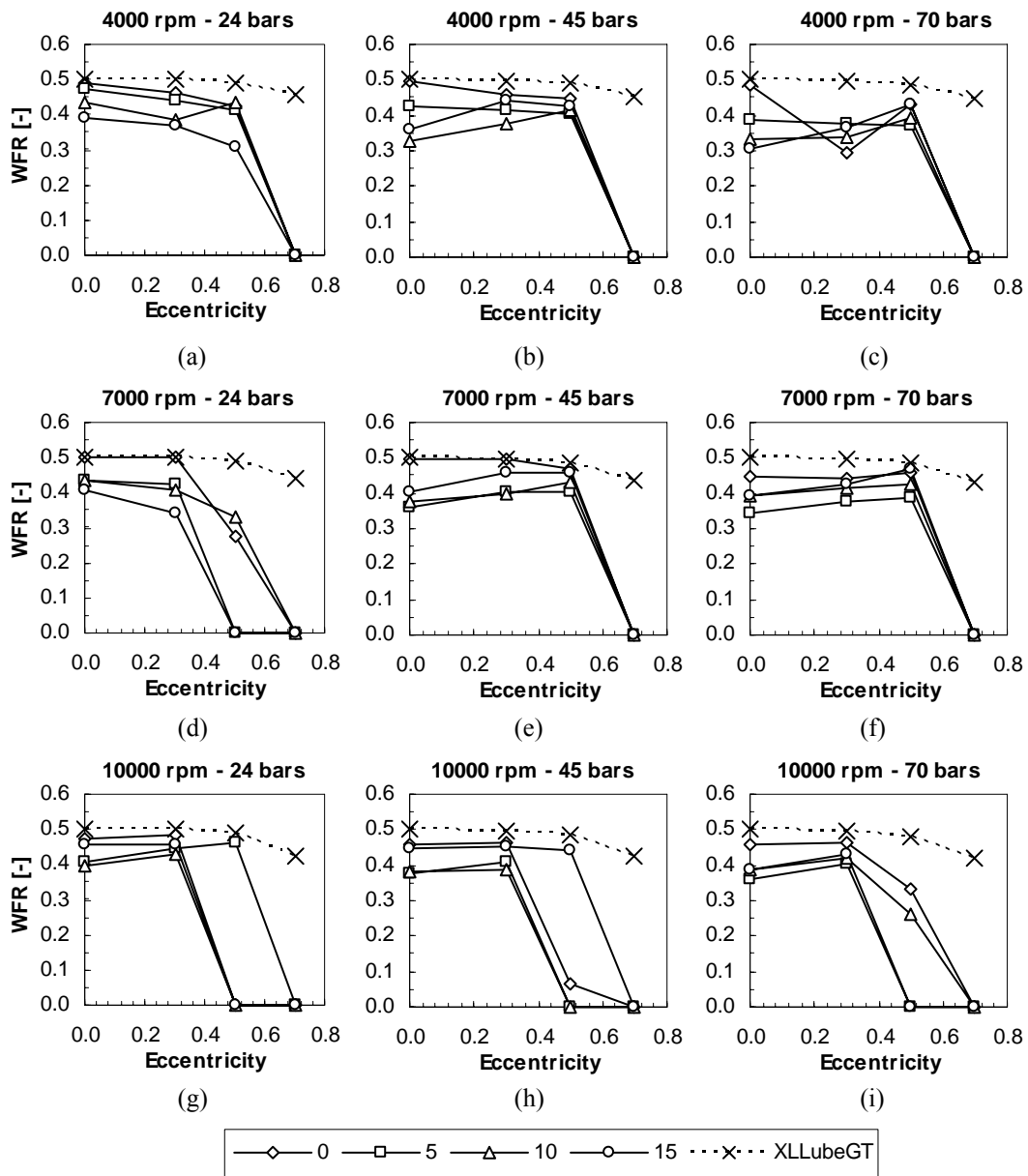


Figure 33. WFR vs. eccentricity for all test conditions of speed, oil inlet pressure, and groove depth

Impact of Clearance on XLLubeGT Predictions

Rotordynamic coefficients and oil leakage are heavily influenced by the seals' clearance. Upon reaching steady state conditions of rotor speed and oil inlet pressure, the rotor radius may increase due to centrifugal growth and thermal expansion. The test seal also experiences thermal expansion. XLLubeGT results shown in Figure 29 through Figure 33 are calculated using the clearance measured prior to testing, which does not include the rotor or seal growth. The impact of centrifugal growth on the rotor radius is determined by [19]

$$\Delta R_r = \frac{1}{4} \cdot \frac{\rho \omega^2}{E} (1 - \nu) \cdot R_r^3 \quad . \quad (25)$$

Additionally, the equation for thermal expansion of the rotor and the seal is

$$\Delta R_{r,s} = R_{r,s} \cdot \alpha_{r,s} \cdot \Delta T \quad . \quad (26)$$

The predicted radial expansion of the rotor due to centrifugal growth and thermal expansion is $3.19 \cdot 10^{-5}$ meters (0.00126"), while the predicted radial expansion of the seal is $3.04 \cdot 10^{-5}$ meters (0.0012"). Therefore, the seal clearance is predicted to decrease 2% from the measured static clearance (a decrease of $1.49 \cdot 10^{-6}$ meters (0.00006")). The thermal expansion of the seal was verified by a re-measurement of the "cold" clearance and a measurement of the seal at a temperature comparable to the oil temperature during testing. Figure 34 and Figure 35 present a comparison of stiffness and damping coefficients with and without predicted considerations of centrifugal growth and thermal expansion. The figures indicate that the rotordynamic coefficients are largely unaffected by the influence of the clearance decrease (results considering growth are denoted in the figure's legend as XLLubeGT_gr). Note that predicted rotor centrifugal growth is

proportional to running speed squared; hence, these predicted small influences are even smaller at 4000 and 7000 rpm.

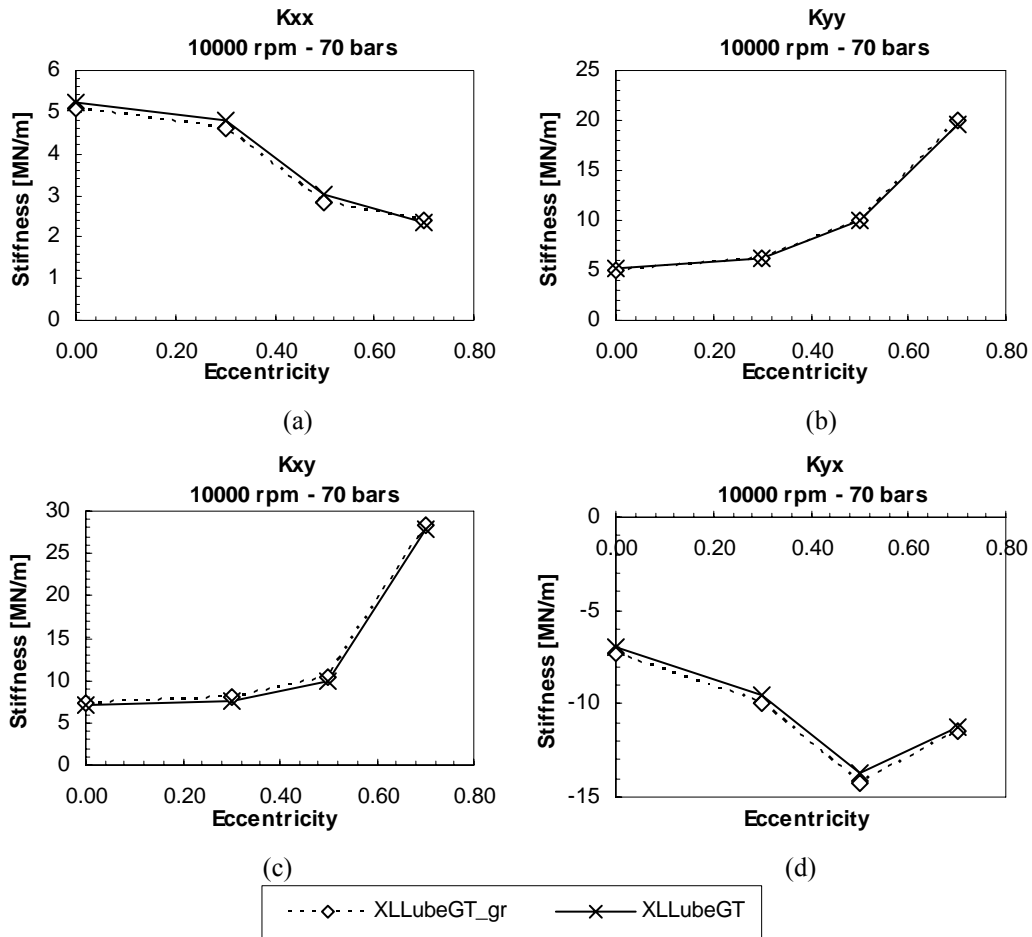


Figure 34. Comparison of direct and cross-coupled stiffness coefficients between XLLubeGT predictions with and without growth analyses

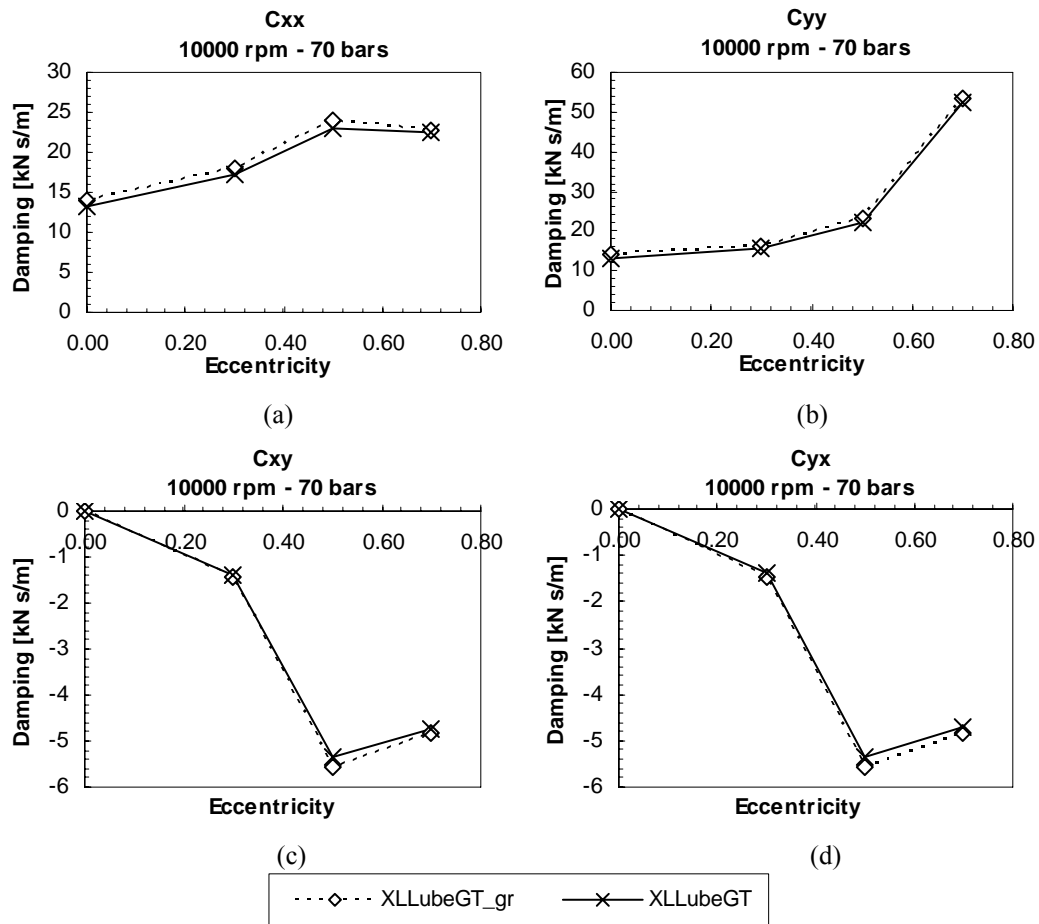


Figure 35. Comparison of direct and cross-coupled damping coefficients between XLLubeGT predictions with and without growth analyses

Seal leakage is also influenced by a change in clearance. Figure 32 shows an excellent correlation between experimental results and XLLubeGT results (based on static clearance measurements). Figure 36 presents seal leakage versus eccentricity for XLLubeGT predictions without considerations of centrifugal growth and thermal expansion, XLLubeGT predictions with those considerations, and experimental data of the test seal with a $Dg/C = 15$. The resulting decrease in clearance with growth considerations leads to the decrease in leakage shown in Figure 36.

With comparable thermal expansion coefficients between the rotor and seal materials, the thermal expansion of the rotor and seal are nearly identical. Thus, the predicted clearance reduction during testing is primarily due to the rotor centrifugal growth. This additional analysis of clearance change during testing results in modestly more accurate XLLubeGT predictions of leakage.

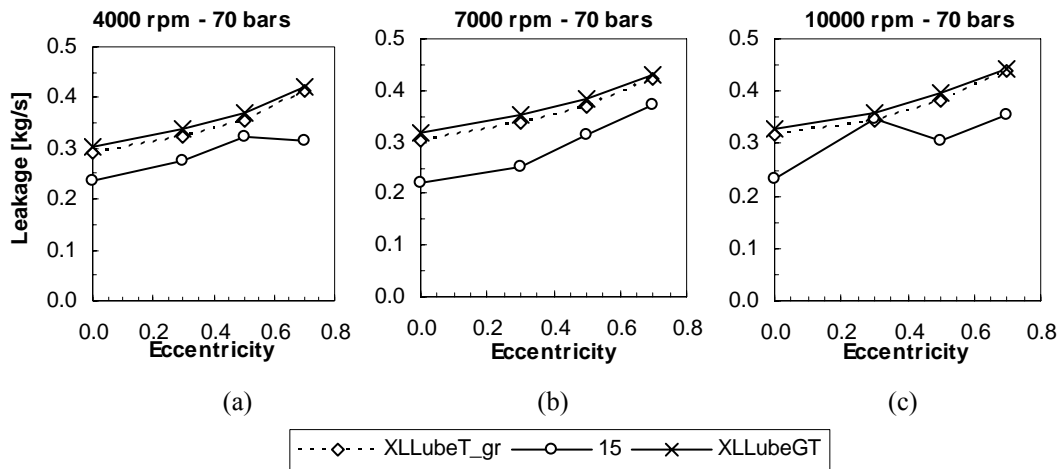


Figure 36. Comparison of seal leakage rates among XLLubeGT predictions with and without growth analyses, and experimental data from $D_g/C=15$

CONCLUSIONS

This thesis provides experimental static and dynamic results for four pairs of seals, including a pair of smooth seals and three pairs of centrally grooved seals. The grooved seals have groove depth-to-clearance ratios (D_g/C) of 5, 10, and 15. Test conditions include three shaft rotational speeds from 4000 to 10000 rpm, three inlet oil pressures from 24 to 70 bars, and seal dimensionless eccentricities from 0 (centered) to 0.7. For each pair of test seals, dynamic results include stiffness and damping coefficients, and static results include stator position, attitude angles, and seal leakage. Stiffness, damping, and leakage are compared among the seal pairs, as well as with a computer code developed by Dr. San Andrés of Texas A&M University, XLLubeGT.

The results of this thesis are used to answer the question: At what groove depth do circumferentially grooved seals become effective in creating separate lands within the seal, yielding negligible pressure perturbations due to rotor motion, and follow XLLubeGT predictions? Experimental results show that oil inlet pressure changes do not affect the seals' rotordynamic coefficients. Stiffness coefficients primarily remain constant through the rotor speed range, though increasing slightly in some cases. Variances in damping are more significant in the low operating speed case. For most test conditions, the stiffness and damping coefficients decrease consistently with increased groove depth; so adding a central groove to a seal does reduce rotordynamic coefficients. However, the magnitude of the decrease is not large enough to correspond to XLLubeGT predictions.

Baheti and Kirk [20] did a thermo-hydrodynamic analysis on the effects of seal groove geometry on rotordynamic coefficients. D_g/C ratios of 5 and 14 were used, which was stated in the paper as common for industrial practice. The analysis details that the larger groove depth effectively breaks up the hydrodynamic pressures across the seal. Results from this thesis show that even the seal with the largest groove depth ($D_g/C=15$) tested does not succeed in creating this effect. For grooved squeeze film dampers (SFD), San Andrés [21] analyzes SFD's with D_g/C ratios of 21.4, 42.85, and 81.75. Results of

this analysis showed a significant reduction in dynamic force coefficients, which may reflect the break-up of hydrodynamic pressures. This would suggest that the groove depth of oil seals needs to be even larger than those tested in this report.

Static results show that seal leakage remains constant among the seals with different groove depths and various rotor speeds, and increases with inlet oil pressure and seal dimensionless eccentricity. XLLubeGT predicts constant seal leakage with rotor speeds and oil inlet pressures, and accurately predicts leakage overall.

Baheti and Kirk [22] suggest that if the seal is operating with large pressure drops across them, then wall flexibility may considerably affect seal rotordynamics. An analysis of seal deformation for those tested for this report showed that the radial displacement of the seal circumference is less than the tolerance specified when machining the seals.

If inertial effects are analyzed for the combination of both seals located inside the stator, and including the gap between the seals (L_{gap}) (see Figure 7), the L/D ratio becomes 0.639. With this larger “total” length-to-diameter ratio, the added mass value is 55 kg. Dividing this result by two (27.5 kg) gives an added mass value for half of the experimentally recorded data (one seal) [23]. This value is the closest to the value obtained through experiments. However, the dynamic pressures were measured at the oil inlet and outlet locations to analyze the effect the gap between the seals has on inertial terms. During shaking, results show no oscillation in pressure from inlet to outlet, indicating that the gap between the seals does not contribute to the large inertial terms obtained.

Recommendations for further investigation in the analysis of groove geometry in laminar oil seals include:

- Test even deeper grooves than those tested in this research effort, which are determined as not deep enough to create the effect of separate lands within the seal.
- Use the same pair of seals for each test groove depth, deepening the groove after each successful test.

- Develop a method for improving the consistency of test conditions including inlet oil temperatures and pressures.

REFERENCES

- [1] Kirk, R.G., 1994, "Analysis and Design of Floating Oil Ring Seals for Centrifugal Compressors," *Proceedings of the 4th International Conference on Rotor Dynamics*, IFTOON, Chicago, pp. 185-190.
- [2] Semanate, J. and San Andrés, L., 1993, "Analysis of Multi-Land High Pressure Oil Seals", *Tribology Transactions*, **36**, No. 4, pp. 661-669.
- [3] Childs, D.W., Phillips, S.G., Rodriguez, L.E., and Al-Ghasem, A., "Experimental Rotordynamic Coefficient and Static Characteristics for Three Laminar Oil Bushing Seals," TRC-SEAL-1-03, Turbomachinery Research Consortium, Texas A&M University, November 2003.
- [4] Kaneko, S., 1984, "Static and Dynamic Characteristics of Annular Plain Seals," *IMEchE*, C278/84, pp 205-214.
- [5] Lomakin, A.A., 1958, "Calculation of Critical Speed and Securing of Dynamic Stability of Hydraulic High-Pressure Pumps with Reference to the Forces Arising in the Gap Seals," *Energomashinostroenie*, **4**, No. 1, p 1158.
- [6] Black, H.F., 1969, "Effects of Hydraulic Forces in Annular Pressure Seals on the Vibrations of Centrifugal Pump Rotors," *J. Mech. Eng. Science*, **11**, No. 2, pp 206-213.
- [7] Black, H.F., and Jenssen, D.N., 1970, "Dynamic Hybrid Bearing Characteristics of Annular Controlled Leakage Seals," *Proceedings of the Inst. Mech. Eng.*, **184**, No. 3N, pp 92-100.
- [8] Black, H.F., and Cochrane, E.A., 1973, "Leakage and Hybrid Bearing Properties of Serrated Seals in Centrifugal Pumps," *Proceedings of the 6th International Conference on Fluid Sealing*, Munich, pp G5-61-70.
- [9] Wilkes, K.W., Kirk, R.G., and Elrod, D.A., 1992, "Rotordynamic Analysis of Circumferentially-Grooved Turbulent Seals: Theory and Comparison to Published Test Results," *Tribology Transactions*, **36**, No. 2, pp. 183-192.

- [10] Hirs, G.G., 1973, "A Bulk-Flow Theory for Turbulence in Lubricant Films," ASME J. Lubr. Tech., **95**, No. 2, pp 137-146.
- [11] Childs, D.W., and Dressman, J. B., 1985, "Convergent-Tapered Annular Seals: Analysis and Testing for Rotordynamic Coefficients," ASME J. Tribol., **107**, No. 3, pp 307-317.
- [12] Iwatsubo, T., and Yang, B.S., 1987. "The Effects of Elastic Deformation on Seal Dynamics," *The 1987 ASME Design Technology Conferences – 11th Biennial Conference on Mechanical Vibration and Noise*, Sep. 27-30, Boston, MA, pp. 435-440.
- [13] Venkataraman, B., and Palazzolo, A.B., 1996, "Effects of Wall Flexibility on the Rotordynamic Coefficients of Turbulent Cryogenic Annular Seals," ASME J. Tribol., **18**, pp. 509-519.
- [14] Kaul, A., 1999, "Design and Development of a Test Setup for the Experimental Determination of the Rotordynamic and Leakage Characteristics of Annular Bushing Oil Seals," M.S. thesis, Texas A&M University, College Station, TX.
- [15] Childs, D., and Hale, K., 1994, "A Test Apparatus and Facility to Identify the Rotordynamic Coefficients of High-Speed Hydrostatic Bearings," ASME J. Tribol., **116**, pp. 337-344.
- [16] Rodriguez, L. E., 2004, "Experimental Frequency-Dependent Rotordynamic Coefficients for a Load-on-Pad, High-Speed, Flexible-Pivot Tilting-Pad Bearing," M.S. thesis, Texas A&M University, College Station, TX.
- [17] San Andrés, L., 2002, *Modern Lubrication Theory*, Class Notes, Texas A&M University, <http://phn.tamu.edu/me626>.
- [18] Reinhardt, E. and Lund, J.W., 1975, "The Influence of Fluid Inertia on the Dynamic Properties of Journal Bearings," ASME J. Lubr. Tech, **97**, No. 2, pp. 159-167.
- [19] Young, W. C., 1989, *Roark's Formulas for Stress and Strain*, McGraw Hill, New York; pp. 703-704.

- [20] Baheti, S.K., and Kirk, R.G., 1995, "Finite Element Thermo-hydrodynamic Analysis of a Circumferentially Grooved Floating Oil Ring Seal," ASLE Trans., **38**, No. 1, pp. 86-96.
- [21] San Andrés, L., 1992, "Analysis of Short Squeeze Film Dampers with a Central Groove," ASME J. Tribol., **114**, No. 4, pp. 659-665.
- [22] Baheti, S.K., and Kirk, R.G., 1999, "Analysis of High Pressure Liquid Seal Ring Distortion and Stability Using Finite Element Methods," ASME J. Tribol., **121**, pp. 921-926.
- [23] San Andrés, L., Personal Communication, Texas A&M Turbomachinery Laboratory, December 12, 2004.

APPENDIX

This appendix contains results previously discussed in this thesis. For the purpose of specifically viewing the comparison between experimental and theoretical results at lower eccentricities, Figure 37 and Figure 38 correspond to Figure 30 and Figure 31, respectively, with the 0.7 eccentricity point omitted.

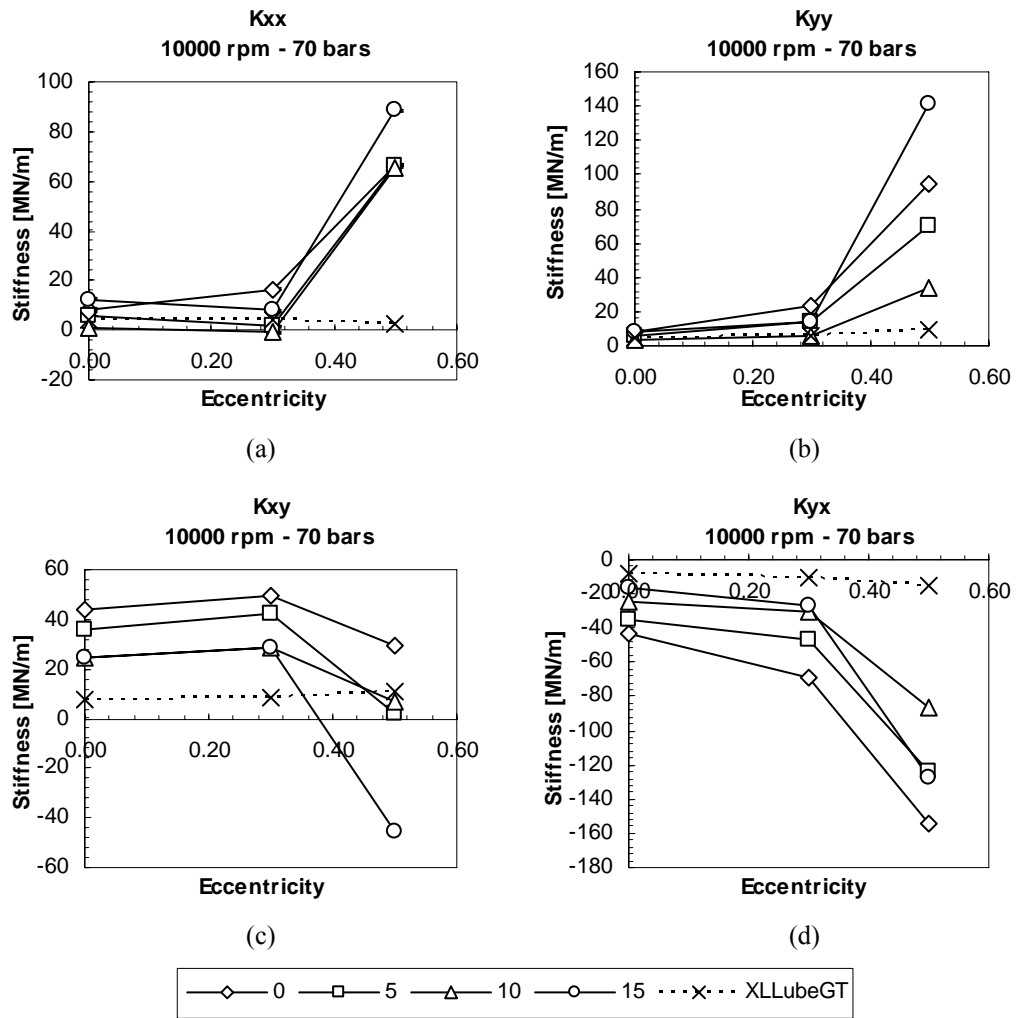


Figure 37. Direct and cross-coupled stiffness coefficients (a) K_{xx} (b) K_{yy} (c) K_{xy} (d) K_{yx} versus eccentricity (0, 0.3, 0.5)

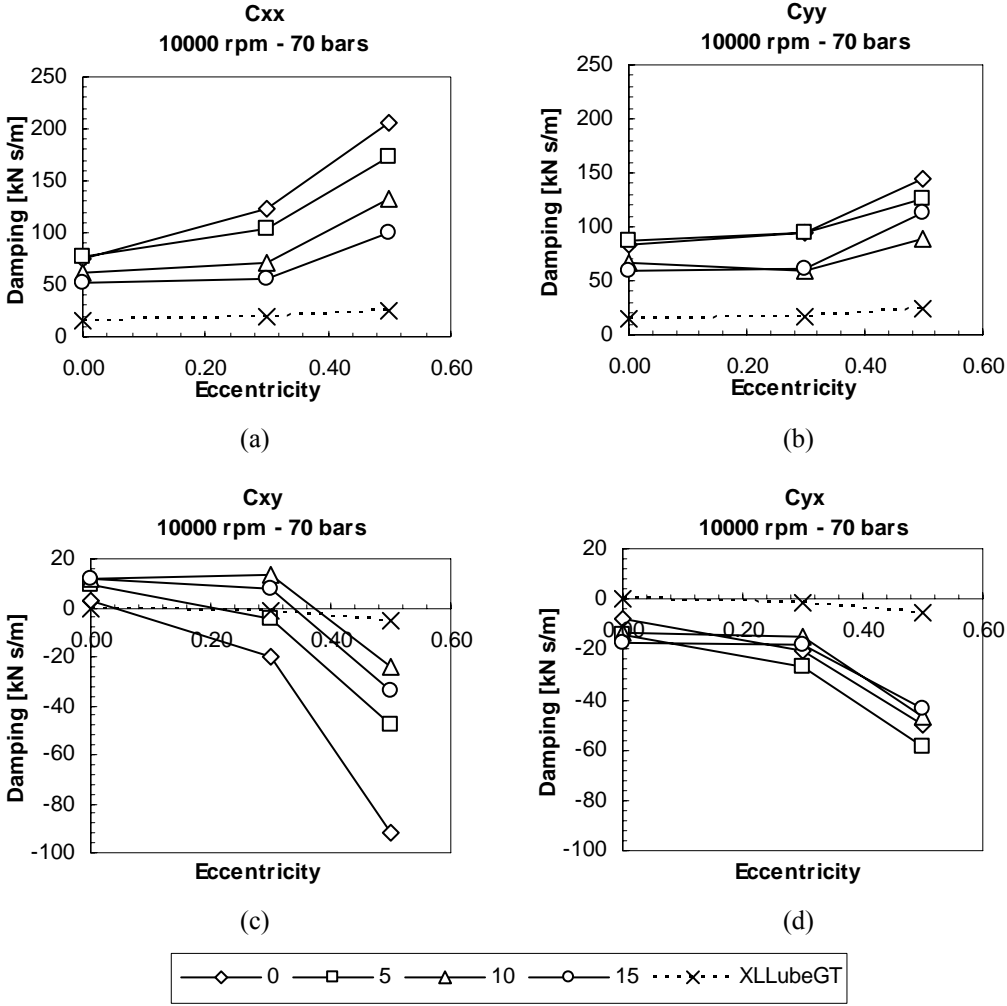


Figure 38. Direct and cross-coupled damping coefficients (a) C_{xx} (b) C_{yy} (c) C_{xy} (d) C_{yx} versus eccentricity (0, 0.3, 0.5)

VITA

Matthew Sheridan Graviss was born on September 3, 1981 in Bethesda, Maryland. He graduated in May 2003 from Auburn University with a Bachelor of Mechanical Engineering degree. He received a Master of Science degree from Texas A&M University in May 2005. He can be reached at the following permanent address:

Matthew Sheridan Graviss
4622 4th Street South
Arlington, VA, 22204